Planetary and Space Science 163 (2018) 14–34

Contents lists available at ScienceDirect

Planetary and Space Science

journal homepage: www.elsevier.com/locate/pss

# Evaluation of Mars probe positioning using X-ray pulsars, celestial, gravity-aided and ground-based measurements

Jiandong Liu [a,b], Shuanggen Jin [a,c,*]

[a] Key Laboratory of Planetary Science, Shanghai Astronomical Observatory, Chinese Academy of Sciences, Shanghai, 200030, China
[b] University of Chinese Academy of Sciences, Beijing, 100049, China
[c] School of Remote Sensing and Geomatics Engineering, Nanjing University of Information Science and Technology, Nanjing 210044, China

ARTICLE INFO

*Keywords:*
Mars probe positioning
X-ray pulsar
Gravity-aided odometry
Optical celestial techniques

ABSTRACT

Autonomous navigation of the Mars probe is a key step for the survivability of the space mission and the success of the scientific experiments. However, Mars probe positioning has large uncertainty due to imprecise techniques and limited observations. In this paper, several key factors of X-ray Pulsar, Optical Celestial, and Gravity-aided navigational system are investigated by the simulation in term of Nonlinear Kalman Filters. The navigational performances are evaluated to investigate the autonomy, accuracy, and stability of the systems. The numbers and the kinds of X-ray Pulsars detected by the antenna system have significant influence on the accuracy and stability of the X-ray Pulsars Navigation (XNAV) system. The XNAV achieves several hundreds of meters orbit accuracy by scanning PSR B1937 + 21, B1821–24 and B0531 + 21 in Earth-Mars cruise orbit. The improvement of pointing-accuracy of the celestial sensor has less effect on increasing accuracy of the Optical Celestial Navigation (OCN) system. The OCN has relatively lower navigation accuracy with a few hundred kilometers but higher stability. For surface rover positioning, we introduce the Gravity-aided Odometry (GAO) and design two algorithms to verify its navigation ability. The accuracy of GAO approximately equals to the performance of the ground-based Radio Tracking (RT). The potential scientific perspectives of above methods are discussed, which could improve the astrophysical and planetary geodetic study.

## 1. Introduction

Since Earth-based Radio Tracking (RT) measurements have some limitations in geometric distribution and visibility for deep-space probes (e.g., Jin et al., 2013; Jin and Zhang, 2014), several autonomous Positioning, Navigation, and Timing (PNT) techniques have been developed to replace or partially replace the ground-based RT systems. Among these PNT methods, the schemes based on X-ray Pulsars, celestial Line-of-Sight and gravity-aid measurements might be helpful due to their passive observation processes (Wei et al., 2013; Liu et al., 2017). However, the key factors to the accuracy, stability, realizability of the systems are not well investigated comprehensively. The scientific applications of these observations and PN results are merely simulated and analyzed to realize astrophysical and planetary geodetic goals.

Firstly, the optical sensors were traditionally boarded on the spacecraft to track the Line-of-Sight of some celestial bodies (Liebe, 2002; Liebe et al., 2016). The measurements have been used to estimate the velocity and position of several deep space probes (Liu et al., 2017; Mortari and Conway, 2017), where the radio tracking system was unavailable. Secondly, the X-ray pulsars (0.1–100 keV), which emits periodic signals recorded by a relatively smaller detector, are available for time keeping as well as navigational beacons by locking their phases or processing the Time Of Arrival (TOA) data (Sheikh et al., 2006; Anderson et al., 2015; Shemar et al., 2016). The positioning accuracy achieved by these periodic beacons is barely attenuated by the increase in distance refer to the reference origin and, to some extent, could determine the orbit autonomously. The X-ray Navigation (XNAV) system have potential to achieve orbit accuracy within 6 km in deep space as far as 100 AU (Shemar et al., 2016). These Precise Orbit Determination (POD) results, especially the non-observable orbit solutions where ground based RT loses tracking, are the fundamental products for Planetary Geodesy in terms of retrieval of gravity field, planet mapping, and atmospheric sounding. Thirdly, the stable gravity field of the terrestrial planets such as Mars is naturally suitable for feature matching positioning for the surface rovers based on gravity observations, which could provide an alternative to current celestial navigation-aided odometry corrected by Vision

* Corresponding author.
*E-mail addresses:* sgjin@shao.ac.cn, sg.jin@yahoo.com (S. Jin).

https://doi.org/10.1016/j.pss.2018.06.014
Received 7 November 2017; Received in revised form 6 March 2018; Accepted 25 June 2018
Available online 26 June 2018

Odometry (VO). The method of gravity matching could give an absolutely positioning to the rover's trajectory which is currently measured by RT. The gravimetric and gradiometric observations are direct measurements for Planetary Geodesy and Geodynamics.

The use of periodic beacons of the Pulsars as timing and navigational signals was first proposed by Reichley et al. (1971) and Downs (1974). The Pulsars selected as navigational beacons should be rotation-powered milliseconds X-ray Pulsars (Chester and Butman, 1981; Becker et al., 2013; Shemar et al., 2016). Many simulations have been done to discuss the XNAV system (e.g., Sheikh et al., 2006; Becker et al., 2013; Anderson et al., 2015; Shemar et al., 2016; Winternitz et al., 2016; Liu et al., 2017), which includes theoretical studies, algorithm designs, and system testing. Recently, several XNAV plans could be candidates for future deep space explorers: The Station Explorer for X-ray Timing and Navigation Technology (SEXTANT) of National Aeronautics and Space Administration (NASA, USA) has been mounted on International Space Station (ISS) in 2017, which the grounding test of the system achieved position and velocity accuracy within 5 km and 10 m/s, respectively (Winternitz et al., 2016). The X-ray Pulsars NAVigation testing satellite-01 (XPNAV-1) launched by China in 2016 has made the observations of Crab Pulsar (PSR B0531 + 21) available for public use (http://www.beidou.gov.cn/xpnavdata.rar) and the Gamma Storm Polarization Detector (POLAR) boarded on TianGong-2 also have detected the Crab X-ray signals which could achieve position and velocity accuracy of 13 km and 300 m/s by using the single Pulsar propagation (Zheng et al., 2017). The Mercury Imaging X-ray Spectrometer (MIXS) instrument of ESA could be a good testing bed for XNAV (Shemar et al., 2016). Currently, the XNAV system can achieve accuracy about ±5 km by single X-ray Pulsar (PSR B0531 + 21 is the most used one) (Becker et al., 2013). This accuracy was extreme striking if the system would board on a spacecraft far away from earth about 30–100 AU. However, most of these simulations or initial results are based on single Pulsar PSR B0531 + 21 due to its strong flux and stable pulse. The accuracy is positive for using in Martian probe navigation compared with the real-time results of RT (Liu et al., 2017). The analysis of the performance of the XNAV with 3–4 Pulsars and their geometric distribution to the system are needed, which could improve the PN accuracy with acceptable observational loads.

The XNAV have extremely vast perspective in booming astrophysics and planetary geodesy researches: The creation of the signal template of XNAV (Appendix A.3), which is to ascertain the key parameters of the Pulsars (Table A.2 of Appendix A.5) that reflects the nature of the celestial body, is a perfect experimental platform to study the characteristics of the Neutron Stars (Winternitz et al., 2016). The signal is also used to keep time with high accuracy, which the time transfer from local to reference scale with POD products can be used to estimate fundamental astrophysical parameters such as Gravitational Constant/Potential of the Solar system (Appendix A.1.). With high accuracy POD ability, the XNAV is a great tool in illustrating the large-scale space-time structure of the solar system and beyond as proposed in Section 4.2. Additionally, XNAV could be the only method which achieves few kilometers or even hundreds of meters POD accuracy as far as 100 AU (Shemar et al., 2016).

The use of Optical Celestial Navigation (OCN) to determine orbit of the spacecraft is still a practical method, even though the XNAV could achieve higher accuracy with complicated hardware in the future (Mortari and Conway, 2017). The OCN has been used in several deep space missions (Mortari and Conway, 2017; Liu et al., 2017), which the basic idea is to track the Line-of-Sight of the celestial bodies by sensors such as star tracker, sun sensor and cameras (Karimi and Mortari, 2015; Liebe et al., 2016; Mortari and Conway, 2017). The accuracy of the position determined by this method approximates a few tens kilometer to hundreds kilometer (Mortari and Conway, 2017). This accuracy could be used in the case of very deep space navigation more than a few tens of AU distance. However, the accuracy would limit the practical application compared with RT techniques in nearby missions like Mars exploration except the OCN could achieve accuracy magnitude within several kilometers or several hundred meters. This means we should reduce the distance between the measured nearby body and the optical cameras, that is, using closer bodies such as moons of the planet. One of the examples is the methodology applied in Mars Reconnaissance Orbiter use narrow Field Of View (FOV) optical camera to capture the two moons of Mars and the background stars (Guinn et al., 2016). The pointing accuracy of these instruments is improved signally in last decades, which achieve accuracy better than one arc second (Liebe et al., 2016). The techniques are still main autonomous navigation method in deep space exploration. The optical cameras, which is not only for the navigation purpose but also for scientific investigations, are used to explore the surface of some planets such as Mars (Maimone et al., 2006). The integrated XNAV/OCN could improve the survivability of the spacecraft.

The use of OCN to determine the Line-of-Sight of celestial bodies or further to track the attitude or heading of the probe is a mature technique (Liebe et al., 2016; Mortari and Conway, 2017). The technique has been applied to positioning the Martian rovers. The processes are as follows (Maimone et al., 2006): The initial trajectory of the rovers is determined by integrated celestial orientation and wheel code counting, synonymously, Wheel Code Odometry (WCO). The Vision Odometry (VO) is used to control the accumulation errors. The absolute position and velocity of the rovers are tracked by ground RT facility or radio ranging between the orbiters and the rovers. Therefore, the absolute PN are separated from the relative trajectory determination, which could generate systematic errors. The complex positioning procedure motivated the interesting for looking new strategies to solve the positioning of the rovers autonomously. The Gravity-aided Odomety (GAO) system has potential to provide stable solution for vehicles under isolated circumstance. The navigation idea uses feature matching based on gravity was initially speculated by Jircitano et al. (1990) for underwater vehicles navigation (Jircitano and Dosch, 1991). The system has been tested and applied to control the errors generated by Inertial Measurement Unit (IMU) system (Odometry) on the underwater vehicles (Rice et al., 2000). The accuracy has been achieved to several hundred meters to few kilometers by using gravimeters to measure the gravity anomaly (Wang et al., 2016a,b; Wu et al., 2017). The accuracy could be improved by using gradiometers to observe the gravity gradient (Wu et al., 2010). The methodology has never been used in surface navigation of Terrestrial Planets such as Mars. The measurements have 3 to 5 mGal uncertainties compared to the background gravity map in the case of underwater vehicles navigation (Wu et al., 2017). The uncertainties could smaller due to the stability characteristic of the planet gravitational field, which makes the matching process easier to converge. The comprehensive analysis of in-situ gravity observations along with the POD products could detect the seasonal gravity field changing due to the Martian $CO_2$ caps sublimation/sedimentation cycles which causes 50% variation in the atmospheric mass. The accurate PNT results of these techniques are fundamental materials for astrophysical and planetary geodetic studies.

The paper focuses on evaluating the accuracy, robustness, advantages, and disadvantages of X-ray Pulsars Navigation (XNAV) system, Optical Celestial Navigation (OCN), Gravity-aided Odometry (GAO), and their integrated navigation form, which are used to estimate the state of the Martian probes. The use of these observations to fulfill some scientific purposes is also simulated and discussed. Firstly, seven X-ray Pulsars (Appendix A.3., Table A2) are selected based on its characteristic which are evaluated together with the performances of the X-ray optics and detector in term of Signal-Noise-Ratio (SNR) to predict the ranging ability of the XNAV (Sheikh et al., 2006; Shemar et al., 2016; Liu et al., 2017). The Pulsars are separated into group of three, four, and seven combinations to evaluate the geometric distribution effect on the orbit determination ability of the Martian probes. The Unscented Kalman Filter (UKF) is used to adjust the data which random noises, clock errors, systematic errors are also considered. Secondly, the ability of the OCN applied in the same orbit is evaluated by integrating XNAV with OCN into a Federal Kalman Filter (FKF). The influence of each subsystem can be controlled by adjust the Information Fusion Factors (IFF). Thirdly, The GAO method is simulated to resolve the absolute location of the Martian

surface rovers. We use Iterated Closest Point (ICP) and Terrain Contour Matching (TERCOM) to match the measurements and the map values. The influences of the gravity map, gravity measurements, and odometry errors on the positioning results are analyzed in term of numeric simulation. Additionally, the observational conditions, advantages and disadvantages of the methods are discussed, especially the potentials of these techniques could be used for improving astrophysical and planetary geodetic research.

The framework of the paper is as follows: The background, development of the techniques, and the forms of the measurements are illustrated in Section 2. Additionally, the accuracy of the XNAV, OCT and GAO are evaluated in terms of numeric simulation in Section 3. The advantages, disadvantages, and the scientific prospects of these techniques are discussed in Section 4. The conclusions are given in Section 5.

## 2. Methods and simulation

### 2.1. X-ray Pulsars Navigation

The navigation scheme of the XNAV is to use the periodical X-ray fluxes emitted from high speed rotation Pulsars as navigational/time-counted beacons (see Fig. 1). Three types observations can be generated based on different algorithms: I) Absolute Navigation (AN) method acquires time delays between the Initial Reference Origin (IRO), e.g., Solar System Barycenter (SSB), and the spacecraft (Sheikh et al., 2006). The TOA to the IRO can be predicted by Taylor expansion of the rotation period or frequency of the Pulsars (Appendix A.3, Equation (A.6)). The TOA to the probe is transferred to Coordinate Time (TC) scale such as Barycentric Dynamical Time (TDB) to complete the comparison (Appendix A.1). The process needs prior orbit information (Appendix A.1-A.3). II) The prior orbit predicted by the dynamical model (Equation (D.1) of Appendix D.1) or other external methods might be not so accurate that could generate errors in observational TOA, which can be fixed by iterated loops to update the locations refer to the TOA pulse in IRO (Appendix A.4). The method is Delta-Correction (DC) (Sheikh et al., 2006; Becker et al., 2013; Shemar et al., 2016). III) The AN and DC method include phase comparison, which the observed pulses are folded according to the periods of the Pulsars to improve the Signal-Noise-Ratio (SNR). The process is time consuming due to the fickle characteristic of the Pulsars. The method designed to lock the Doppler Effect (DE) caused by approaching or leaving the Line-of-Sight of the Pulsars is Phase Doppler Locking Loop (PDLL) (Golshan and Sheikh, 2007; Anderson et al., 2015). The velocity is estimated from the Doppler Effect and then integration for position (Appendix A.2).

The Delta-Correction is suitable for single Pulsar navigation (Shemar et al., 2016), which reduce the systematic errors by differencing the Absolute Navigation equation (Appendix A.3, Equation (A.8)) to estimate the position and velocity by iterated method (Becker et al., 2013). The PDLL could achieve orbit accuracy within 10 km by continue phase locking (Wang and Zhang, 2016). We adopt Absolute Navigation to simulate the XNAV for the convenience of simulation: The AN measurement is easy to generate. The navigational Pulsars can be formed into several groups to approach the practical situation which the numbers of the visible Pulsars are changing during the cruising of the spacecraft. The geometric distributions of the Pulsars on the performance of the XNAV is also evaluated by these combinations.

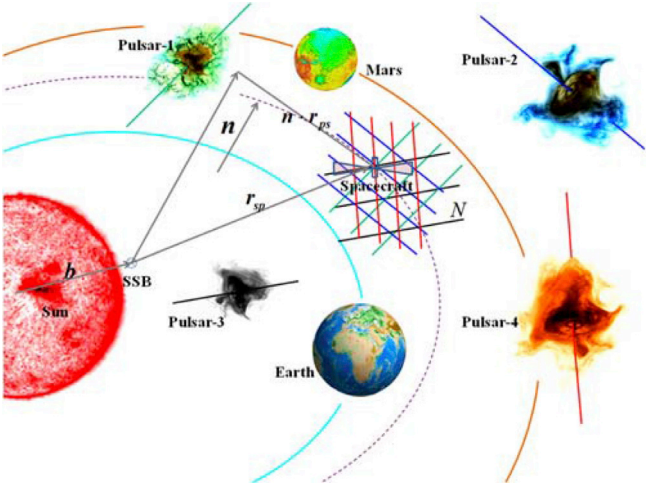


**Fig. 1.** Absolutely Navigation of XNAV by multiple X-ray Pulsars. The solution to solve the ambiguity N is also depicted. The mathematic and physical models are explained in Appendix A.

### 2.2. Optical Celestial Navigation

The onboard optical sensors/cameras of the spacecraft acquire Line-of-Sight (LS) of the celestial bodies as well as establish angular observations or track LS changing rate to estimate the position and velocity of the probe (Liebe et al., 2016; Mortari and Conway, 2017), which is called Optical Celestial Navigation (OCN). The methods require at least one nearby bodies to keep the observations varying along with the movements of the spacecraft (Mortari and Conway, 2017). The techniques are suitable for attitude keeping due to its accurate LS observations (Liebe et al., 2016). As successful applied in several deep space missions (Centinello et al., 2015), the methods could provide autonomous navigation solutions when the ground-probe telecommunication was unavailable (Liu et al., 2017).

For orbit determination, the ground-based RT techniques achieves more accurate solutions than OCN does. However, the method is still used in practice especially when the ground-spacecraft communication link is sheltered by the celestial bodies. The stability of the OCN has been proved by simulations and practices (Centinello et al., 2015; Liu et al., 2017; Mortari and Conway, 2017). The integrated XNAV/OCN is beneficial to both the accuracy and stability to the navigational scheme. We use angular observations in this paper (Appendix B).

### 2.3. Gravity-aided odometry

The main idea of the Gravity-aided Odometry (GAO) is to find the optimal trajectory $\widehat{\rho}$ by minimizing the difference between the observed gravity values $g_l$ and the background values $g_r$ provided by the gravity map and extracted from the initial trajectory$\rho$:

$$\widehat{\rho} = \text{argmin}(f(g_l - g_r, \rho)) \quad (1)$$

The algorithms designed to fulfill the equation (1) include Iteration Closest Points (ICP, Appendix C.1), Terrain Contour Matching (TERCOM, Appendix C.2) and Sandia Inertial Terrain Aided Navigation (SITAN) (Rice et al., 2000) (see Fig. 2). The former two are for static analysis and vice versa of the latter. The $g_l$ and $g_r$ can be gravitational anomalies measured by gravimeter or gravity gradients acquired by gradiometer. For Mars Exploration Rover (MER), the locations of the rovers are deduced by odometry: The heading of the rovers is determined by tracking the Line-of-Sight of Sun (OCN). The travel distance is recorded by Wheel Coding Odometry (WCO). The trajectory acquired by the integrated method would generate divergence due to the systematic errors. Thus, Visual Odometry (VO) is implemented to control the growth of the biases in term of feature tracking of photo pairs (Maimone et al., 2006). The navigational methodologies include RT, OCN, WCO, VO, and GAO are pictured in Fig. 2.

As illustrated in Fig. 2, the absolute positioning of the rovers is complex and separated from the relative trajectory deduced by combining OCN, WCO and VO, which can be replaced by GAO. The simulation use MER trajectories and Martian Gravity Map 2011 (Liu et al., 2018) to simulate the gravity anomaly measurements. There are no

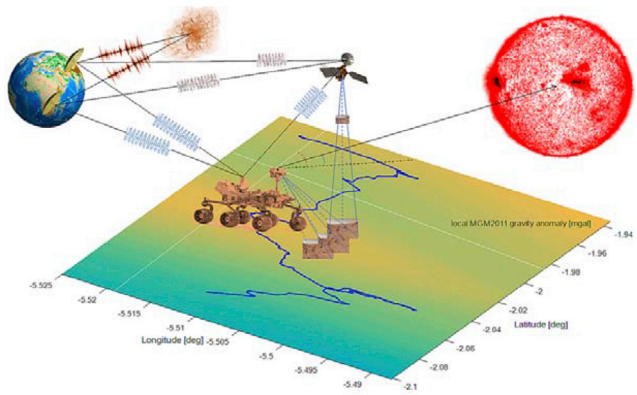


**Fig. 2.** The navigational propagations of the Martian surface rover. The absolute position and velocity of the rover is determined by Radio Tracking technologies which include radio ranging/ranging rate (Unified S/X Band, ground-rover or orbiter-rover), time delay (Very Long Baseline Interferometry), and range difference (Delta-DOR). The results are verified by feature comparison of images which is taken from orbiter and the rover, respectively. The observing of Sun determines the heading of the rovers and the wheel code system counts the distance, which the integrated form is a dead-reckon odometry. The GAO could be another absolute positioning method for the rovers.

such instruments onboard the rovers. Thus, the noises added to the observations are based on experiments in the surface of earth. The use gravity gradient for GAO could achieve relative higher accuracy in the case of underwater vehicles navigation (Wu et al., 2010). But the simulation configuration is more complex to generate. The stable gravity field of Mars is suitable for acquiring anomaly measurements. The complicated external variables to the GAO for Mars rovers has been analyzed by Liu et al. (2018). This paper focus on compare the different matching algorithms on the convergence of the navigational system as well as analysis of GAO observations and results in scientific applications.

## 3. Scenarios and results

This section uses numeric simulation to evaluate the positioning and navigation ability of XNAV, OCN, and GAO for probes and rovers. We adopt absolutely navigation algorithm for XNAV for the convenience of simulation. The angle distance has been adopted to simulate the OCN system. We use static matching methods to evaluate the positioning accuracy of GAO. The emphasizes are as follows: The geometric distribution of Pulsars on the performance of XNAV as well as impact of signal losing on the stability of the system; the verification of the stability of integrated XNAV/OCN system; the results comparation of two static algorithms on GAO.

### 3.1. Evaluation of XNAV in cruise orbit determination by combined pulsars

#### 3.1.1. Simulation configurations of XNAV

Seven X-ray Pulsars are selected as navigational beacons (Table A2 of Appendix A.5) due to their outstanding signal quality as illustrated by Equation (A.13) of Appendix A.5. These Pulsars are rotation-powered millisecond X-ray Pulsars which have been used as navigational candidates by most of XNAV simulations and experiments (Sheikh et al., 2006; Becker et al., 2013; Anderson et al., 2015; Shemar et al., 2016). These Pulsars are most suitable signal sources, especially B0531 + 21 is the most frequent used beacon. The Pulsars are grouped into three types combinations (Table A4 of Appendix A.5) to avoid the inadequacies of current simulations and experiments, which run to the extreme such as single Pulsar navigation use Delta-Corrections or multiply Pulsars navigation (Shemar et al., 2016; Liu et al., 2017). The single Pulsar navigation is vulnerable to the initial trajectory (dynamical model) due to its iteration loop. The parameters can be estimated are limited due to the insufficient measurements. For the multiply Pulsars navigation, the excessive Pulsars will certainly introduce observational problems to the detector. For PDLL method, the loss of phase locking would generate gross navigation errors. Therefore, the combinations of 3/4 X-ray Pulsars for XNAV navigation have advantages both in reducing scanning burden and increasing the stabilities/accuracy of the system.

We use Absolute Navigation (Appendix A.3) to simulate the XNAV. The simulation configurations are illustrated in Table 1. The observations are simulated by nominal orbit information based on Equation (A.8.) of Appendix A.3. Then, we use UKF to adjust the measurements and the orbital dynamical model (Appendix D.1). We use Fortran 77 format to program the routines. The mixture process of errors in terms of observational noises, clock biases, and other delay corrections are implemented by these subroutines and functions. The program is also used to simulate OCN and integrated XNAV/OCN system by using Federal Kalman Filter (FKF) (Appendix D.2). The orbital dynamical model includes solar gravitational forces (main), Earth and Mars perturbations. The expression is illustrated in Equation (D.1) of Appendix D.1. Details are described in Liu et al. (2017).

#### 3.1.2. Pulsars geometric distribution on XNAV performance

The combinations of the Pulsars are based on the ranging accuracy as illustrated in Table A3 of Appendix A.5. The combinations in Table A4 are comprehensive consideration in terms of loads of the detector and the ranging ability (which equals to the prior orbit determination accuracy the XNAV can achieve) of the Pulsars. For 3-Pulsars combinations, the best accuracy is achieved by the combination PSR B1937 + 21, B1821-24, and B0531 + 21 as is predicted by the precision analysis using Equation (A.13) of Appendix A.5. The simulation configurations are as Table 1. This case only includes the observational noise $v_\tau$ and clock biases $\delta t_c$ in Equation (A.8) of Appendix A.3. The clock offset $a_0$ equals to $10^{-11}\,s$ and the clock drift $a_1$ is $10^{-12}\,s/s$, which have limited influence on the orbit determination performance for Martian cruise orbit (Liu et al., 2017). We adopt sigma parameters (Equation (D.2) of Appendix D.1) $\alpha = 0.1$, $\beta = 2$, and $\kappa = 0.01$. We have done a few hundreds of simulations to make sure the sigma parameters are appropriate for the UKF. As it is demonstrated by Liu et al. (2017), the parameters $\beta$ and $\kappa$ have limited influence on the convergences of the algorithm as well as $\alpha = 0.1$ is the most stable case. Fig. 3 illustrates the orbit determination errors between the nominal orbit and the UKF solution. The position errors are within 310 m and the velocity errors are within 2 m/s. The challenges which the XNAV system faces to achieve such high accuracy will discussed in Section 4.1.1. The influence of systematic errors is unconsidered.

The group of PSR B0540–69, J0205 + 6449 and J0437-4715 achieves the worst orbit accuracy as predicted by the ranging errors. The results are portrayed in Fig. 4. The observations are mixed with clock biases and

**Table 1**
Simulation Conditions and configurations of XNAV system & integrated XNAV and OCN system.

| Models& Conditions | Configurations |
|---|---|
| Dynamical Model | Main force (Sun)+Earth/Mars perturbations + noises |
| Observational Model | Absolutely Navigation/Star Light Distance |
| Orbit Integration Method | Runge-Kutta8 (7) |
| Observational Interval | 864 s |
| Integration Step | 1 s |
| Mission Duration | 100 days |
| Dynamical Ephemeris | DE405 |
| Adjustment Method | Unscented Kalman Filter/Federal Kalman Filter |
| Reference System | J2000 Inertial Heliocentric Coordinate System (J2000IHCS) |
| Time Scale | UTC + TDB |
| Nominal Orbit Model | Dynamical Model + Radiation Model + orbit maneuvers |
| Clock Model | First order of offset and drift model |
| Estimated Parameters | Position/Velocity (in J2000IHCS) |

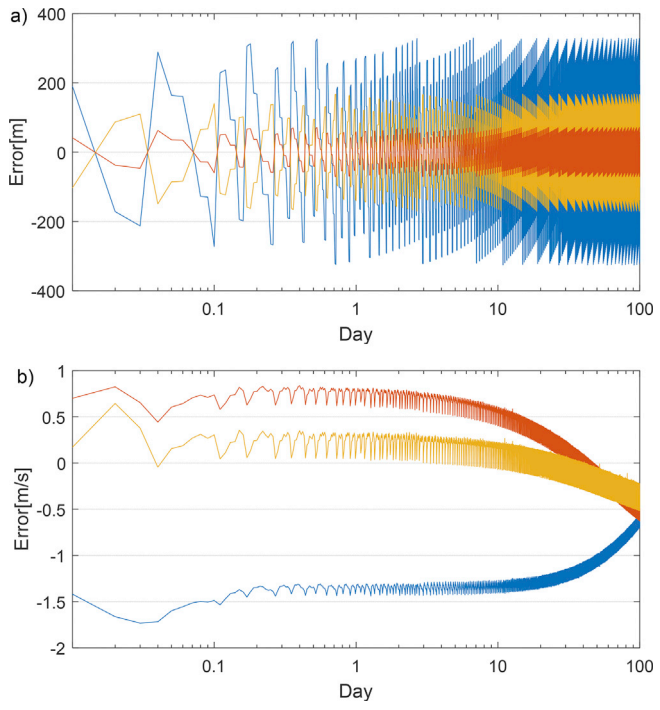


**Fig. 3.** Orbit accuracy determined by PSR B1937 + 21, B1821–24 and B0531 + 21 (Group *T-a* in Table A4 of Appendix A.5). a) position error. b) velocity error. The blue, red and yellow represent errors in X, Y, Z directions, respectively. The errors are differences between the nominal orbit and the results from UKF. We use basic statistics in terms of maximum, minimum, mean, and Standard Deviation (SD) to evaluate these errors in the following tables (The clock biases of this figure are $a_0 = 10^{-11}\,s$ and $a_1 = 10^{-12}\,s/s$). (For interpretation of the references to colour in this figure legend, the reader is referred to the Web version of this article.)

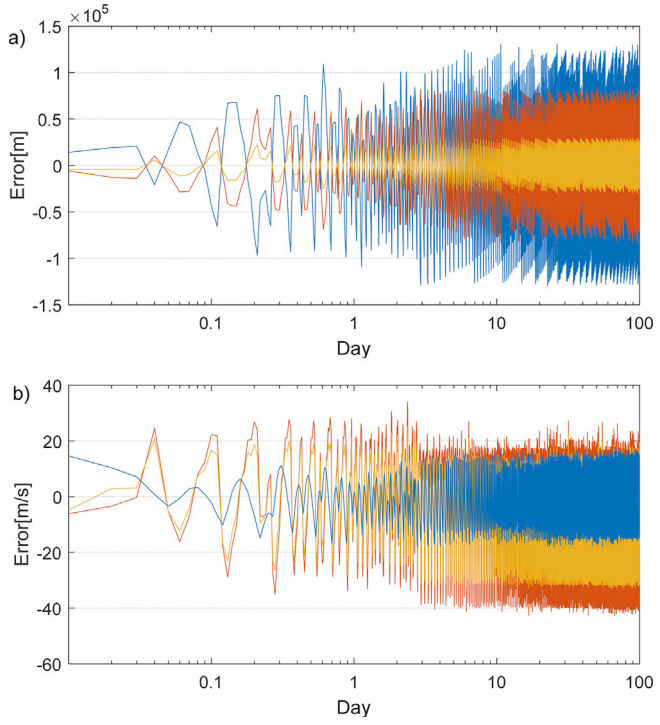


**Fig. 4.** Orbit accuracy determined by PSR B0540–69, J0205 + 6449 and J0437-4715 (Group *T-c* in Table A4 of Appendix A.5).

random noises as instructed by the Absolutely Navigation equation. The clock offset $a_0$ is set to $10^{-9}\,s$ and the drift parameter $a_1$ is set to $10^{-10}\,s/s$. Other parameters are the same as the best group. The accuracy achieved by this combination is 120 km in position and 40 m/s in velocity. Other two groups of 3-Pulsar performances are illustrated in Figure A2 and Figure A3 of Appendix 6.

The accuracy of orbit determination by 3-Pulsars is shown in Table 2. The position errors vary from 350 m to 130 km and velocity errors vary from 2 m/s to 45 m/s. The observations have been mixed with the clock errors and random noises. The offset and drift of the clock are listed in Table 2. The random noises are simulated based on observational time equals to 864 s and effective detector area is 0.5 $m^2$. The results show the differences between the errors evaluated by different X-ray Pulsars are observably. The best groups (*T-a* and *T-b*) achieve few hundred meters accuracy. The medium group (*T-d*) is of within 3 km. The worst combination approximates 130 km. The combinations constructed by any other 3-Pulasrs are worse than the group shown in Table 2, since the ranging errors of these seven X-ray Pulsars are the top-7 predicted by the evaluation Equation (A.13) of Appendix A.5.

The clock biases set in Table 2 have minor influence on the accuracy of the orbit determination during the 100 days simulation if the orbit errors worse than kilometers (Liu et al., 2017). However, the setting could generate systematic perturbations which would influence the results of the system. Fig. 5 shows the errors of the UKF solutions experience a long-term drift which can be fitted by first order Polynomial. The errors have an upper tilt at end of the epoch compared with Fig. 3. In turn, we can use this group of Pulsars to detect the clock uncertainties or to estimate the parameters of the clock model. The Precise Orbit Determination (POD) of spacecraft by XNAV should consider the clock biases.

As it has been shown in Table 2, the orbit determination errors by the 3-Pulsars combinations are not stable. The errors changed dramatically when the target Pulsar is different, which could be from hundred meters to hundred kilometers. The accuracy can be improved by adding more observations to the UKF. We use two groups of 4-Pulsars combination to simulate the orbit determination. The results are shown in Table 3. The PN results are illustrated in Figure A3 and Figure A.4 of Appendix A.6. The combinations provide limited improvement for the best case of 3-Pulsars combination (*T-a*). However, it can improve the worst cases (*T-c*) tremendously. The position and velocity errors could be achieved within 2.5 km and 15 m/s, respectively. As it shows in Figure A.5 and Table A5 of Appendix A.6, increasing in the Pulsars numbers can improve the navigation accuracy due to the improvements of the observations and better positioning geometry. The different types of X-ray Pulsars used in the propagation also have influence on the accuracy as shown in Table A5. All other results of XNAV are shown in Appendix A.6.

### 3.1.3. *The impact of observed signal/targets fluctuating on XNAV*

The increase or decrease of the number of X-ray Pulsars equals to simulate the signal capturing/losing events. As illustrated in Figure A.5 and Table A5, the system achieves 250 m and 2 m/s accuracy with full signal of seven Pulsars. For the worst case, the losing of three Pulsars signal will reduce the accuracy to 2.5 km and 12 m/s as illustrated in Figure A.3. The signal PSR J1208 + 4232 breaks off from the *F-b* combination will cause extremely deterioration of the XNAV system, which the PN accuracy will collapse to 130 km and 45 m/s as shown in *T-c* of Table 2 and Fig. 4. The best/worst accuracy achieved by single-Pulsar navigation using DC algorithm is 4.7/70 km, respectively (Shemar et al., 2016). The observed Targets have major impact on the performance of XNAV.

The switchover of observed targets within certain combinations equals to simulate the signal fluctuation during the cruising of the spacecraft. For 3-Pulsars combinations, the scanned signals switch among the *T-a*, *T-b*, *T-c*, *T-d* causes severe accuracy fluctuations, which the accuracy varies from 350 m & 2 m/s to 130 km & 45 m/s as shown in Table 2. The perturbations will certainly give a significant impact on the XNAV system, which would cause unitability of the XNAV system as well

**Table 2**
Orbit uncertainty in position (m) and velocity (m/s) by 3-Pulsars in X, Y, and Z direction. The accuracy in magnitude of kilometer is special noted in km. The Group name can be seen in Table A4 of Appendix A.5.

| *T-a* | | | | *T-b* | | | | *T-c* | | | | *T-d* | | | | |
|---|---|---|---|---|---|---|---|---|---|---|---|---|---|---|---|---|
| $a_0 = 10^{-9}s$ | | | | $a_1 = 10^{-10}s/s$ | | | | $T = 864\,s$ | | | | $A = 0.5\,m^2$ | | | | |
| max | min | mean | SD | max | min | mean | SD | max | min | mean | SD | max | min | mean | SD | |
| 359.4 | −320.7 | 19.5 | 188.6 | 596.3 | −588.7 | 2.2 | 341.0 | 130.31 km | −130.30 km | −199.7 | 64.04 km | 1951.7 | −1938.1 | 16.8 | 1120.7 | X |
| 76.6 | −69.9 | 3.4 | 41.0 | 321.1 | −323.8 | −2.3 | 186.2 | 83.04 km | −83.02 km | 128.2 | 40.70 km | 1322.9 | −1321.8 | 7.2 | 762.6 | Y |
| 166.4 | −182.3 | −8.1 | 97.6 | 646.9 | −647.3 | 1.7 | 374.2 | 29.99 km | −30.00 km | 47.14 | 14.79 km | 2475.0 | −2482.6 | −16.3 | 1430.5 | Z |
| −0.54 | −1.58 | −1.02 | 0.23 | −0.46 | −2.16 | −1.03 | 0.25 | 16.56 | −22.99 | −1.03 | 9.51 | 0.17 | −2.66 | −1.03 | 0.47 | VX |
| 0.85 | −0.60 | 0.00 | 0.36 | 1.00 | −0.87 | 0.00 | 0.37 | 32.06 | −42.03 | −0.01 | 19.10 | 1.82 | −1.91 | 0.00 | 0.58 | VY |
| 0.43 | −0.47 | −0.09 | 0.17 | 1.78 | −0.97 | −0.09 | 0.27 | 25.06 | −32.79 | −0.10 | 14.36 | 2.13 | −2.84 | −0.09 | 0.87 | VZ |

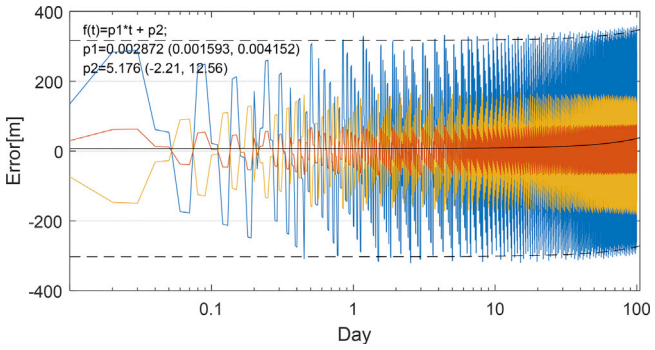


**Fig. 5.** Clock biases on the performance of the XNAV solutions. Orbit accuracy determined by PSR B1937 + 21, B1821–24 and B0531 + 21. Clock biases have been mixed into the observations as described in Table 2. The errors have long term drift caused by the clock biases.

as collapse of the UKF. The oscillation of the XNAV accuracy can be steadied by increasing the observed Pulsars as shown in Table 3 and Table A5 of Appendix A.6. However, this will increase the observational burden of XNAV.

### 3.2. Integrated XNAV and OCN for cruise orbit determination

#### 3.2.1. Essential and information factor design of the integrated system

As it shown in section 3.1.2 and section 3.1.3, the orbit accuracy achieved by XNAV varies dependent on the target Pulsars and the numbers of measurements can be detected. Therefore, the accuracy of the XNAV would change dramatically in short time if the above two factors have changed. The OCN system provided stable navigation ability which is necessary to aid the XNAV when the latter suffers perturbations due to loss of signal, phase jumps, and changing of observed Pulsars. The tracking of Line-of-Sight of celestial targets by sensors is a mature technique nowadays. The OCN has been verified by several missions as autonomous navigational method which provides independent position and velocity information to the spacecraft (Centinello et al., 2015). We use UKF to simulate the XNAV and OCN subsystem. The effectiveness of the single or integrated system has been proved by computer simulation (Liu et al., 2017; Mortari and Conway, 2017).

The two UKFs are combined by the Federal Kalman Filter (FKF) to simulate the integrated navigation system. The infused information adjusted by the FKF is from the UKF results of the subsystem (Equation (D.3) of Appendix. D.2). The importance of the XNAV and OCN is weighted by the Information Fusion Factors (IFF) as described in Equation (D.4) of Appendix D.2. The ratio of IFF calculated based on the adjustment covariance of each subsystem is about XNAV/OCN ≈0.83/0.17 for the seven Pulsars case (Liu et al., 2017), where the parameters for Sigma Point Sampling (Equation (D.2) of Appendix D.1) are set to $\alpha = 0.1$, $\beta = 2$, and $\kappa = 0.01$. The variances $P_{XNAV}$ and $P_{OCN}$ of the estimations can be adjusted via changing the values of α, β, and κ. Once the variances adjusted, the IFF of the subsystem changed. We have repeated the routines for several ten times, which found for $\beta = 2$, and $\kappa = -3$ the XNAV to OCN ratio changed from 0.83/0.17 to 0.14/0.86 when α moved from 0.1 to 0.125. When the system fulfills the former ratio, the orbit determination accuracy basically equals to the XNAV system. On the contrary, the latter ratio indicates the integrated system have similar performance with the OCN system. The purpose of the section is to evaluate the navigation performance of the OCN for Martian probe, therefore, the α is set to 0.125 to improve the IFF of the OCN subsystem. The propagations of the integrated system is shown in Table 1. The pointing accuracy of sensors of the celestial bodies is listed in Tables 4 and 5. The simulation of the OCN observations is described in Appendix B.1.

**Table 3**
Orbit uncertainty in position (m) and velocity (m/s) by 4-Pulsars in X, Y, and Z directions.

| | *F-a*/B1937 + 21 & B1821-24 & B0531 + 21 & J0218 + 4232 | | | | *F-b*/B0540-69 & J0218 + 4232 & J0205 + 6449 & J0437-4715 | | | |
|---|---|---|---|---|---|---|---|---|
| | $a_0 = 10^{-9}s$ | | $a_1 = 10^{-10}s/s$ | | $T = 864$ s | | $A = 0.5\,m^2$ | |
| | max | min | mean | SD | max | min | mean | SD |
| X | 357.0 | −320.1 | 18.4 | 189.5 | 1919.3 | −1916.7 | 9.8 | 1095.3 |
| Y | 76.1 | −69.9 | 3.1 | 41.2 | 2107.6 | −2110.4 | −6.38 | 1208.8 |
| Z | 166.4 | −181.1 | −7.5 | 98.1 | 426.2 | −426.5 | −1.91 | 242.5 |
| VX | −0.33 | −1.82 | −0.77 | 0.23 | 1.86 | −8.83 | −0.77 | 0.94 |
| VY | 0.94 | −0.45 | 0.11 | 0.35 | 11.44 | −6.39 | 0.11 | 3.12 |
| VZ | 0.38 | −0.44 | −0.12 | 0.17 | 5.43 | −3.85 | −0.11 | 1.91 |

**Table 4**
The orbit uncertainty (position *km*, velocity *m/s*) evaluated by integrated OCN and XNAV with three Pulsars.

| T-a/OCN | | | | T-b/OCN | | | | T-c/OCN | | | | T-d/OCN | | | | |
|---|---|---|---|---|---|---|---|---|---|---|---|---|---|---|---|---|
| $a_0 = 10^{-9}$s | | | | $a_1 = 10^{-10}$s/s | | | | T = 864 s | | | | $A = 0.5\,m^2$ | | | | |
| [Pointing accuracy of stars sensors, sun sensors, and planets sensors are equal to 1″,10″, and 0.005°, respectively.] | | | | | | | | | | | | | | | | |
| max | min | mean | SD | max | min | mean | SD | max | min | mean | SD | max | min | mean | SD | |
| 222.16 | 5.64 | 220.46 | 5.40 | 224.26 | 6.60 | 220.44 | 5.59 | 428.72 | −19.87 | 220.32 | 74.91 | 232.79 | 1.00 | 220.45 | 7.01 | X |
| 220.86 | 6.56 | 219.37 | 5.37 | 223.34 | 5.61 | 219.36 | 5.55 | 506.28 | −6.49 | 219.44 | 96.13 | 232.06 | 1.13 | 219.37 | 7.05 | Y |
| 219.92 | 7.00 | 218.39 | 5.34 | 222.92 | 5.27 | 218.37 | 5.55 | 487.10 | 1.03 | 218.41 | 90.68 | 233.03 | 6.95 | 218.39 | 7.46 | Z |
| 14.59 | −1.57 | −1.01 | 0.60 | 13.19 | −2.07 | −1.01 | 0.66 | 52.23 | −49.17 | −1.03 | 22.64 | 16.10 | −4.20 | −1.01 | 1.47 | VX |
| 16.46 | −0.78 | 0.03 | 0.69 | 15.79 | −1.22 | 0.03 | 0.77 | 59.12 | −48.75 | 0.02 | 25.34 | 18.36 | −3.08 | 0.03 | 1.53 | VY |
| 15.94 | −0.62 | −0.03 | 0.59 | 15.36 | −1.05 | −0.03 | 0.70 | 57.71 | −48.89 | −0.05 | 24.77 | 17.12 | −2.99 | −0.03 | 1.54 | VZ |

**Table 5**
The orbit uncertainty (position *km*, velocity *m/s*) evaluated by integrated OCN and XNAV with four Pulsars.

| | F-a/OCN B1937 + 21 & B1821-24 & B0531 + 21 & J0218 + 4232 | | | | | F-b/OCN B0540-69 & J0218 + 4232 & J0205 + 6449 & J0437-4715 | | |
|---|---|---|---|---|---|---|---|---|
| | $a_0 = 10^{-9}s$ | | | $a_1 = 10^{-10}s/s$ | $T = 864$ s | $A = 0.5\,m^2$ | | |
| | [Pointing accuracy of stars sensors, sun sensors, and planets sensors are equal to 1″,10″, and 0.005°, respectively.] | | | | | | | |
| | Max | min | mean | SD | max | min | mean | SD |
| X | 221.81 | 6.19 | 220.46 | 5.44 | 251.11 | 10.25 | 220.46 | 13.03 |
| Y | 220.70 | 4.73 | 219.37 | 5.37 | 260.44 | −7.14 | 219.37 | 18.56 |
| Z | 219.71 | 4.74 | 218.38 | 5.37 | 254.53 | 3.21 | 218.39 | 15.89 |
| VX | 13.55 | −1.61 | −1.01 | 0.57 | 18.28 | −9.96 | −1.00 | 3.79 |
| VY | 16.44 | −0.66 | 0.03 | 0.70 | 25.42 | −10.58 | 0.03 | 4.51 |
| VZ | 15.68 | −0.48 | −0.03 | 0.59 | 22.14 | −9.93 | −0.03 | 4.19 |

### 3.2.2. *Performances of the integrated XNAV/OCN system*

Compared with the XNAV system, the integrated system converges slower as shown in Fig. 6, Figure B.1, and Figure B2 of Appendix B.2. The huge accuracy difference between XNAV and OCN leads to incompatible of the adjustment covariance of each subsystem in the UKF and FKF routines. The performance of the integrated OCN/XNAV with three Pulsars are illustrated in Figs. 6 and 7 and Table 4. The system takes 0.25 days to converge to the steady state for combination *T-a*/OCN, *T-b*/OCN, and *T-d*/OCN. For combination *T-c*/OCN, the convergence speed is relative faster due to the same level navigation performances of XNAV and OCN, which both have hundreds of kilometers accuracy. For all cases there, the position accuracy is worse than 215 km and the velocity accuracy is worse than 15 m/s. As shown in Table 5, the increase of the numbers of the Pulsars will not improve the accuracy of the integrated system. The IFFs of the integrated system are dominated by the OCN subsystem as specified in section 3.2.1.

The accuracy of the OCN keeps the same of the worst case of XNAV, which makes the combination *T-c*/OCN easer to converge as shown in Fig. 7. The calculated IFF according to Equation (D.4) of Appendix D.2 can influence the converge time of the Kalman Filters. The problem could be solved by adoptive algorithms. The final accuracy will not be influenced by the converge time, which verified by Table 4, Table 5. All other results are illustrated in Appendix B.2. The OCN system have positive effect on steadying the XNAV performance in the integrated system as shown in Tables 4 and 5. The signal switchover and the observed numbers of Pulsars causes minor impact on the integrated system.

### 3.2.3. *The X-ray detectors and optical cameras*

The vast geometric distribution of the navigational X-ray Pulsars requires point antenna to collect multi-Pulsars photons. As listed in Table A2 of Appendix A.5, most of the Pulsars are weak sources with fluxes less than 10 ph $cm^{-2}s^{-1}$, which asks for larger collecting areas. The optics used by astrophysics observatory are collimated devices (Shemar et al., 2016). However, the background X-ray noises will decrease the Signal-Noise-Ratio (SNR) of the observations. On this hand, the noises should be shield with small focal plane optics, synonymously, the concentrator. The strategy has been adopted by SEXTANT (Winternitz et al., 2016). Currently, the Silicon Drift Detector (SDD), which is made of silicon PIN diodes that the single X-ray photons can trigger enough electronics and holes to generate strong voltage signals, is designed to detect the concentrated X-ray photons with effective areas less than 0.3 $m^2$ (Okajima et al., 2016). The antenna system should also fulfill the practical requirements such as low mass, small volume, and less power consumption (Prigozhina et al., 2012).

As mentioned before, the Star sensor could maintain the attitudes of

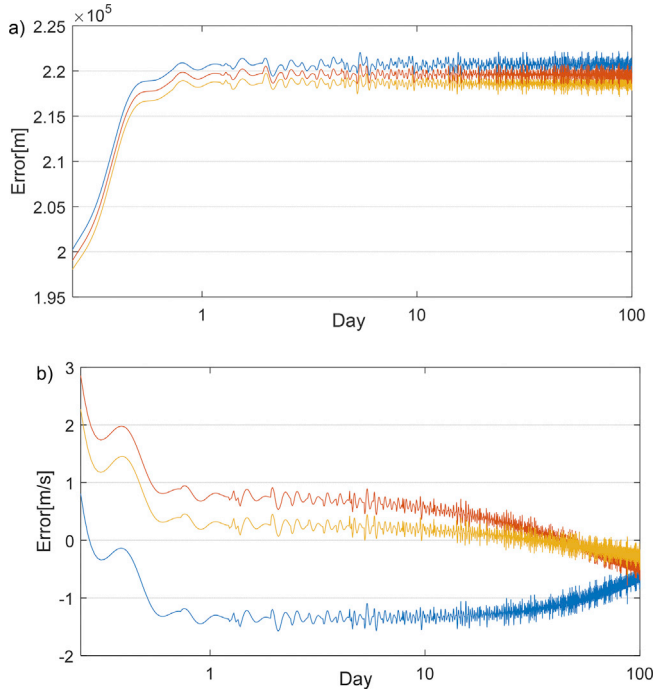


**Fig. 6.** Orbit accuracy determined by integrated XNAV and OCN, which the XNAV includes PSR B1937 + 21, B1821–24 and B0531 + 21.

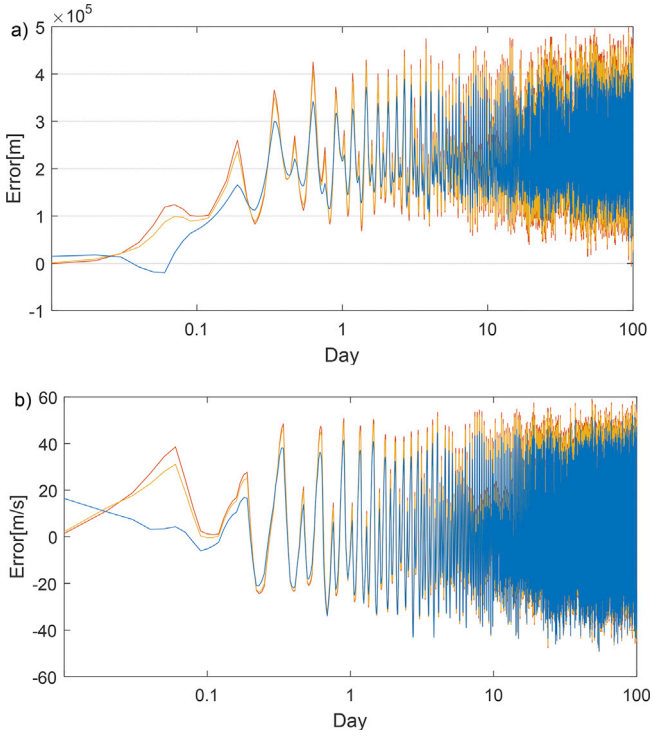


**Fig. 7.** Orbit accuracy determined by integrated XNAV and OCN, which the XNAV includes PSR B0540–69, J0205 + 6449 and J0437-4715.

satellite. For our XNAV/OCN system, the Star camera can be integrated into the X-ray antenna system to track the light-of-sight for the attitudes as well as navigational observations. The SEXTANT has adopted this design (Winternitz et al., 2016). The propagation uses optical cameras with narrow Field Of View (FOV) to scan the nearby body and its background stars is applied in MRO missions. The integrated light-of-sight observations from all types sensors are piratical to implement by algorithms. The pointing accuracy of the Star sensor is better than 1″ nowadays. For Sun and Planet sensor, the accuracy approximates 10″ (Liebe et al., 2016; Liebe et al., 2016). The main error source is the uncertainties existed in the extracting of the center of the celestial body image. The improvement of pointing accuracy of the hardware has minor influence on the orbit determination performance, which the distance between the reference origin and the spacecraft causes huge errors (Liu et al., 2017). This can be explained by analyzing the Equations (B.1) and (B.2) of Appendix B.1 in term of law of error propagation. The results shown in Tables 4 and 5 have verified the stable performance of the OCN system.

### 3.3. Surface rover positioning by GAO

#### 3.3.1. Simulation conditions of GAO

The travel trajectories of the surface Rover of Mars have high relative accuracy. The Gravity-aided Odometry could provide another positioning solution besides RT to fix the absolute locations of the traverse points. The relative trajectory deduced by above Odometry is assumed as one of the initial inputs to the comparison algorithm. The Spirit rover, which roves about 3 km, includes 393 way-points deduced by WO and VO have relative accuracy within 1 m. The number of the waypoints of the Opportunity rover is 1068. The trajectories are assumed to be the true traverse. The simulated traverse is generated by Equation (C.1) of Appendix C.1, which the simulated gravity anomaly is mixed with errors up to 2 mGal (difference between measurements and the map values) and 0.01 mGal noises (the resolution of a gravimeter). The 0.002° noises equal to 100 m position noises. The spatial resolution of the gravity map is 3′ × 3′, which the mean distance between two traverse points is 0.017′. The gravity maps we used were developed by Hirt et al. (2012), which were based on MRO110B2 gravity model and MOLA topography. ICP and TERCOM are implemented to search the optimal matched trajectories. The algorithms are summarized in Appendix C. The initial trajectory is smoother than our simulated trajectory, which suggests the random errors added in the paper are larger than practical case which applied in MER rovers. The aim of the scheme is to test the robustness of the matching algorithms.

#### 3.3.2. Results by ICP and TERCOM

The results are illustrated in Fig. 8 and Fig. 9. TERCOM have better performance than ICP, which the former is more stable for matching. The similar gravity anomaly variation at some specific area could cause mismatching when the ICP algorithm is implemented. The positioning errors grow with the distance increase. For underwater case, the problem is solved by SITAN algorithm, in which the Kalman Filter is integrated with TERCOM to complete the matching and position updating (Wang et al., 2016a,b). The random uncertainties of the trajectory can be controlled by the VO. The diversity of the gravity field around Opportunity is rougher than the areas around Spirit, which is shown in Figs. 8

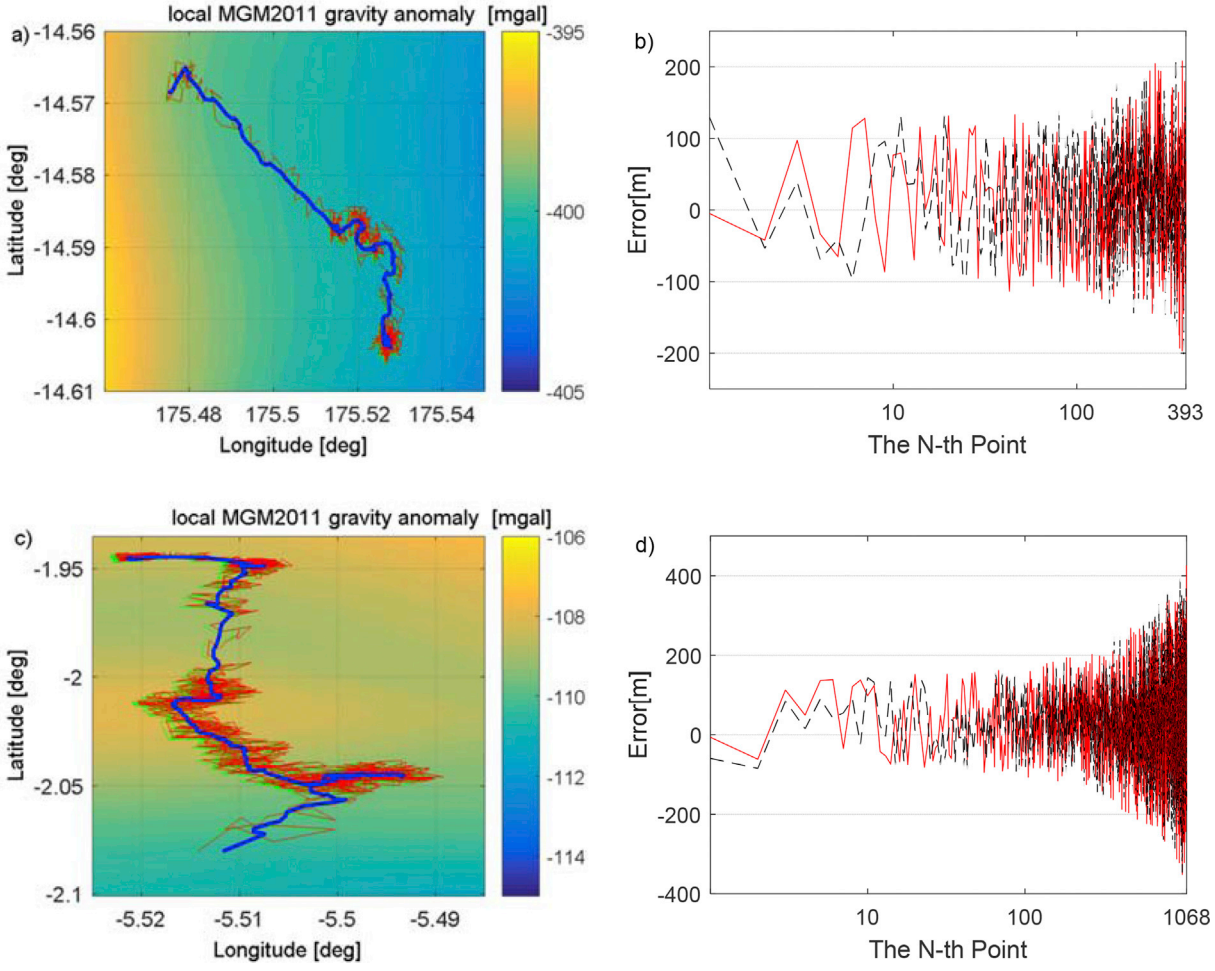


**Fig. 8.** The positioning performance of GAO evaluated by TERCOM.

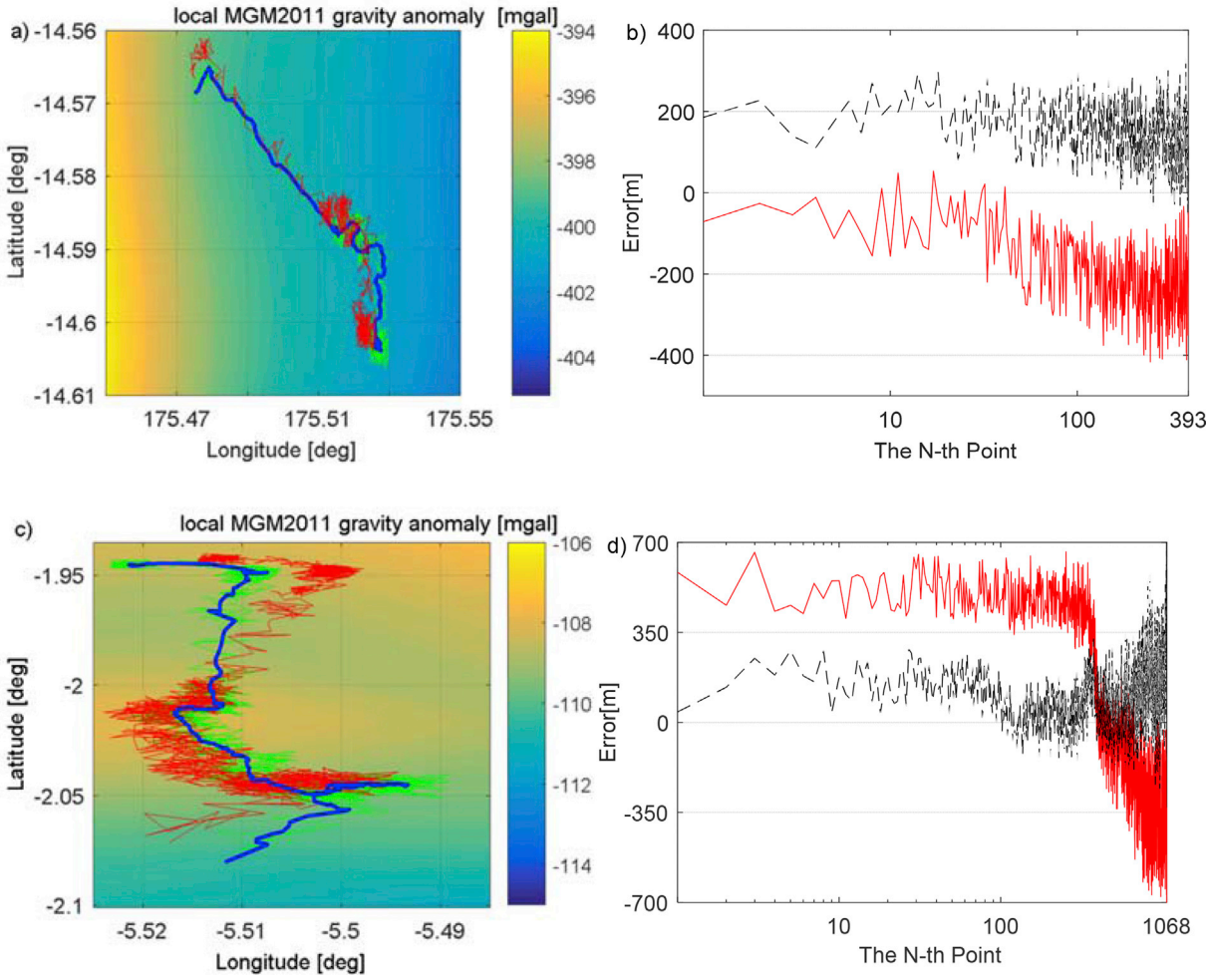


**Fig. 9.** The positioning performance of GAO evaluated by ICP.

and 9. We have done the matching process for several ten times, which the TERCOM always obtains higher accuracy.

The resolution of the gravity map should be improved, which the MGM2011 could only provide $3' \times 3'$ map (Hirt et al., 2012). The lower resolution causes increase in differences between instrument measurements and the map. The gravity map retrieved from POD products or terrestrial ground-based gravity observations can improve the map, which decreases the differences. The odometry provided by traditional method in terms of WCO, VO could afford accurate relative trajectory for the rover, whose random errors added to the initial trajectory will be eliminated.

The accuracy of the GAO is positive if the future gravity map can fulfill the matching requirements. The performance of TERCOM is more stable if the initial trajectory has been deduced by relative navigation method in terms of wheel odometry, celestial heading, and VO. The ICP might be suitable in shape keeping of the original traverse. The TERCOM are more suitable in combining with real-time updating navigational method such as Kalman Filter. The complex variables to performance of the GAO system was investigated by Liu et al. (2018) by using ICP matching method. The advantage of the GAO is the method can integrate all relative results compactly deduced by OCN, WCO, and VO with gravity observations.

### 3.4. Ground-based radio tracking and other methods

#### 3.4.1. Spacecraft tracking by RT

The Ground-based Radio Tracking includes ranging, ranging rate, and angular measurements measured by Unified S/X Band (USB) Radar (nowadays most of the tracking missions use X band) or Radio Telescope which is traditionally used for Very Long Baseline Interferometry (VLBI). The USB realizes ranging or ranging rate of the probes in high precision as 1 m and 1 mm/s nearby Mars (Martinmur et al., 2011; Yan et al., 2017). The ranging measurements are combined in terms of Delta-DOR and Multiply-Way Doppler Observation (MWDO), which achieves 4 km position accuracy for distance 1 AU away from ground station (Becker et al., 2018; Liu et al., 2017). The precision of the time delay/delay rate observations of VLBI achieves 10 picosecond magnitudes (Yan et al., 2018). The integrated of the USB and VLBI achieves positioning accuracy at several tens meters to hundreds of meters for Mars orbiter (Martinmur et al., 2011; Yan et al., 2018). The newly research reports the RT could provide positioning results for orbiters at several tens meters and even meters/decimeters level for landers (Yan et al., 2018).

#### 3.4.2. Rovers navigation

The navigational strategies of Mars rovers are pictured in Fig. 2. The absolute locations of the rovers are tracked by MWDO, which mainly includes the first couples of days when the probes were landed on the surface of Mars. The landing sites are also captured by cameras aboard on the orbiter, which the image features are extracted to compare with the topographic points taken by the rovers' cameras. As portrayed in Table 6, the differences between the RT and the method are within 350 m (Liu et al., 2018). Currently, the Same-Beam VLBI technique are applied to tracking the distance between the lander and the rover, which the accuracy approximates 10 m (Yan et al., 2017, 2018). The relative trajectory deduced by VO has high accuracy within 1 m.

**Table 6**
Positioning results of GAO compared with other techniques (Liu et al., 2018).

| Positioning techniques and bias | MER-A (Spirit) | | MER-B(Opportunity) | |
|---|---|---|---|---|
| Radio Tracking [deg] | 175.47848°E | 14.571892°S | 354.47417°E | 1.9483°S |
| Photograph Feature (PF) | 175.4729°E | 14.5692°S | 354.4734°E | 1.9462°S |
| Position bias [deg] | 0.00558° | 0.002692° | 0.00077° | 0.0021° |
| Position bias [m] | 330.68 m | 159.53 m | 45.63 m | 124.49 m |
| GAO [deg] | 175.4774399°E | 14.56667786°S | 354.473670131°E | 1.944713097°S |
| Bias compared with RT [deg] | 0.001040113° | 0.005214136° | 0.000499869° | 0.003586903° |
| Bias compared with RT [m] | 61.60 m | 308.82 m | 29.61 m | 212.45 m |
| Bias Compared PF [deg] | −0.004539887° | 0.002522136° | −0.000270131° | 0.001486903° |
| Bias Compared PF [m] | −268.89 m | 149.389 m | −16.00 m | 88.07 m |

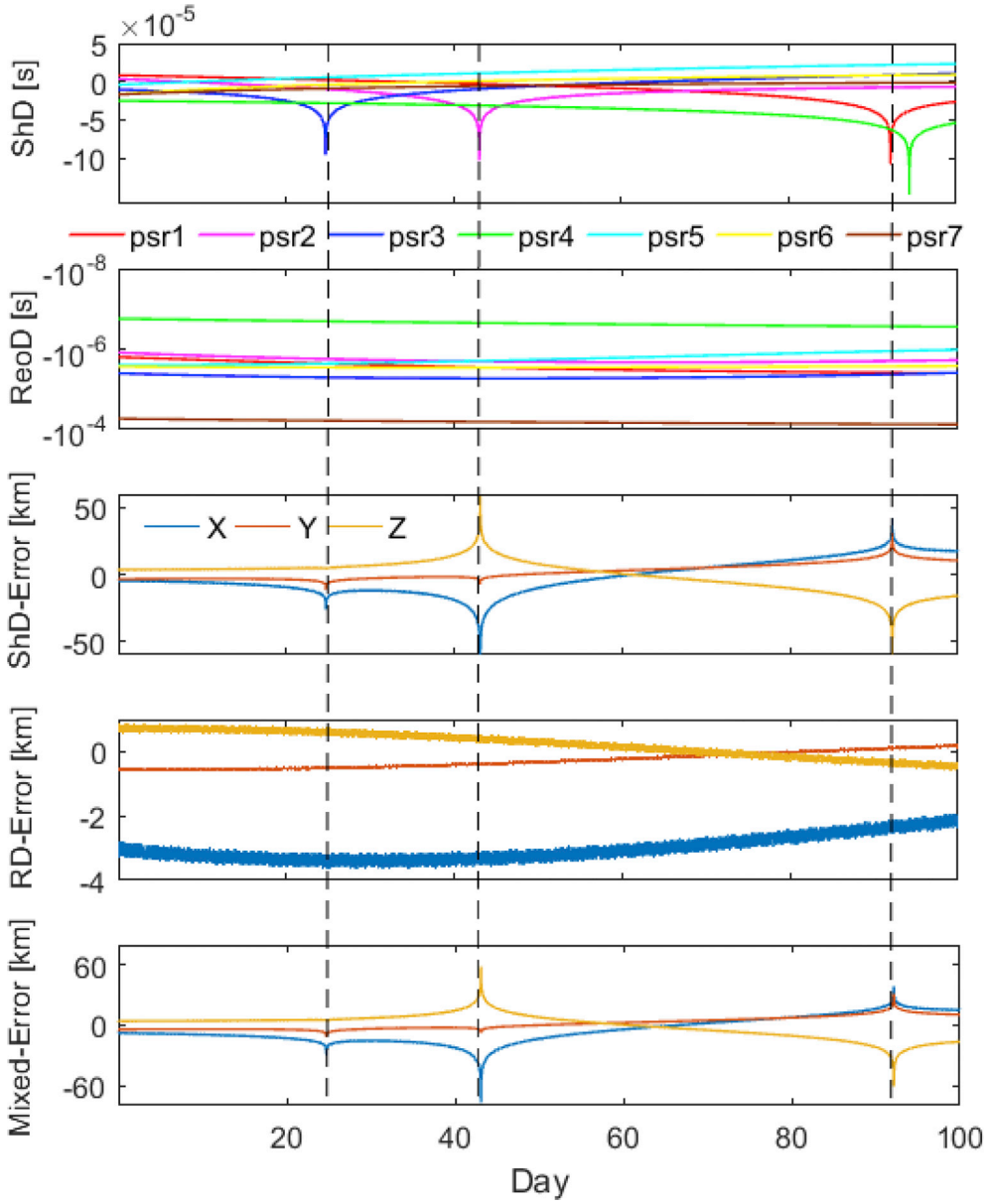


**Fig. 10.** The effects of Shapiro Delay (ShD) and Reomer Delay (RD) on orbit determination accuracy. Top panel: Shapiro Delay; Second panel: Reomer Delay; Third panel: ShD effects on orbit accuracy; Fourth panel: RD effects on orbit accuracy; Bottom panel: Mixture effects.

## 4. Discussions and prospects

### 4.1. The limitation of the techniques

#### 4.1.1. Scanning challenges of XNAV system

The orbit determination performances of the XNAV for Martian spacecraft use Absolute Navigation algorithm are depended on the Pulsars and its geometric distribution used in the navigation schedule as shown in Section 2.2.1. It is possible for the XNAV to achieve hundreds of meters position accuracy and several meters per second velocity accuracy (Figs. 2 and 3 and Tables 2 and 3). The increase of the navigational Pulsars could improve the accuracy and stability of the system as shown

in Table 3. However, the Pulsars which have excellent characters are limited according to the Table A2 and Table A3 of Appendix A.3. Current XNAV research and simulations are highly relied on PR B1937 + 21, B1821-24, and B0531 + 21. The XNAV missions such as SEXTANT and XPNAV-1 should focus on searching, recording, and evaluating new X-ray Pulsars which have period of millisecond, stable and strong in fluxes, and well-distributed.

The practical use of the XNAV has several hardware requirements must face: The X-ray optics and detectors system for interplanetary missions should be integrated compact to reduce the load. Currently, the size of the detector can be less than 0.3 $m^2$ for both SEXTANT and XPNAV-1 (Mitchell et al., 2015; Okajima et al., 2016). As shown in Table A2 of Appendix A.5, the fluxes of some Pulsars are so dim ($<$10 ph $cm^{-2}$ $s^{-1}$) that use relative smaller detector even cannot extract the navigational bacons from the background X-ray flux ($\approx$5 ph $cm^{-2}$ $s^{-1}$ $sr^{-1}$). The X-ray optics used by SEXTANT and XPNAV-1 are concentrators (Winternitz et al., 2016), which are possible to scanning dim X-ray Pulsars. The Silicon Drift Detector (SDD) is suitable for single X-ray photos detection (Prigozhina et al., 2012), which could be a direction for future XNAV system (Shemar et al., 2016). To reduce the load of the spacecraft, XNAV signal detection system are required to design as point antenna. The use of such antenna would bring new challenges which receive beacons from widespread Pulsars on the celestial sphere. Some low elevating angle observations should be rejected from the measurements (Zheng et al., 2017).

#### 4.1.2. Limitations of OCN

The positioning accuracy of spacecraft by tracking the Line-of-Sight of the celestial bodies is about hundreds of kilometers as shown in Section 2.2.2. The OCN dose has several limitations, even though the technique is in practical use and the performance is stable. Firstly, the lower accuracy compares with radio tracking (Mortari and Conway, 2017; Liu et al., 2017). The lower orbital determination accuracy leads to difficulty in scientific parameters estimation, which would limit the scientific application of the OCN data. Currently, the star sensor could achieve pointing accuracy of 1 arcsecond and for the sun sensor the accuracy is about 10 arcseconds (Liebe et al., 2016). The accuracy for absolute navigation using these angles and changing rate of angles is still limited due to the large distance between the celestial bodies and sensors. The discordant accuracy performance between XNAV and OCN results in slowly convergence of the integrated system as shown in Fig. 5. Secondly, the scanning of the nearby celestial bodies, e.g., Planets and its satellite, would rely on several sensors (this paper) or Narrow FOV optical navigation camera as implemented by MRO missions. For Mars Cruise orbit, the accuracy is within 300 km as shown in Fig. 5. The accuracy could be improved nearby the celestial body but the invisible of the targets could leads to system deterioration.

#### 4.1.3. Challenges of GAO

The installation of the gravimeter or gravity gradiometer into Martian rovers or probably surface vehicles of some terrestrial Planets has never been implemented except for Earth. The gravity maps of the Martian are retrieved from Precise Orbit Determination (POD) products. The in-situ surface gravity observations can also improve the quality of the map. The resolution of the map can be improved by multiply measurements in the case of Earth. The improvements of Martian gravity map are needed. Currently, the resolution of the Martian gravity anomaly map is $3' \times 3'$(Hirt et al., 2012). The retrieval accuracy approximates few tens mGal, which is impossible for GAO in Mars. The gravity gradient might be not accurate to implement the matching.

The observational circumstance of terrestrial planet is stable that the perturbations caused by mass transfer might be minor. The relative gravity is measured by gravitometer with one sample per seconds achieves accuracy within 0.01 mGal (Liu et al., 2018). The gradiometer is more suitable to conduct GAO due to its high accuracy (within several tens E) and comprehensive measurements (Wu et al., 2010). The two instruments are always compact integrated into the Universal Navigation Module (UNM) to reduce the volume and power consumption (Rice et al., 2000). The requirements of rover GAO for the UNM should be with high accuracy and lower mass and volume, which theses consumptions should be approximating to the Hazard Cameras system of MER, which is possible in near future.

### 4.2. Scientific prospective

#### 4.2.1. XNAV in astrophysics and planetary geodesy

The orbit determination ability of XNAV, OCN and GAO for Martian probes proved in Section 2.2 shows the techniques have potential in providing navigation information for interplanetary scientific missions. As shown in Fig. 10, the Shapiro Delay is about $10^{-4}$ to $10^{-5}$ $s$ and the Reomer Delay is about $10^{-4}$ to $10^{-7}$ $s$, which the effects on the orbit determination accuracy is about $\pm$50 km and within 4 km, respectively. In turn, some combinations of XNAV in Section 2.2.1 shown in Tables 4 and 5 can be used to estimate the effects, which equal to depict General Relativity and Interstellar Medium influences. This also means the XNAV can be used as a space or planetary astronomical observatory to research and define the time-space structure as illustrated in Fig. 11. The XNAV are also proposed to detect low-frequency gravitational waves (Becker et al., 2017). The XNAV could provide higher accuracy ranging measurements for astronomical observation than ever before. The maximum points illustrated in Fig. 10 is due to the Shapiro effects which are calculated by Equation (A.8) of Appendix A.3.

As shown in Figs. 3–6, our simulation indicates the appropriate arrangement of 3 or 4 navigational X-ray Pulsars could achieve PN accuracy within 360 m with accurate atomic clocks to keep the time system. The POD results in such accuracy are not only suitable to estimate the clock biases but also can use these navigational information as references for other scientific goals if we use XNAV to determine the mission orbits of Mars explorers. The XNAV works well when the satellite is invisible due to its autonomous advantage. As illustrated by Shemar et al. (2016), our errors will increase to few kilometers in distance as far as 100 AU. Thus, the POD results would be beneficial to astrophysics and planetary geodesy than ever before, which could provide precise ranging measurements traditional ground-based RT cannot reach. The navigational system, which includes coordinates-time transfer among different space-time frames, is also suitable to link these reference datums.

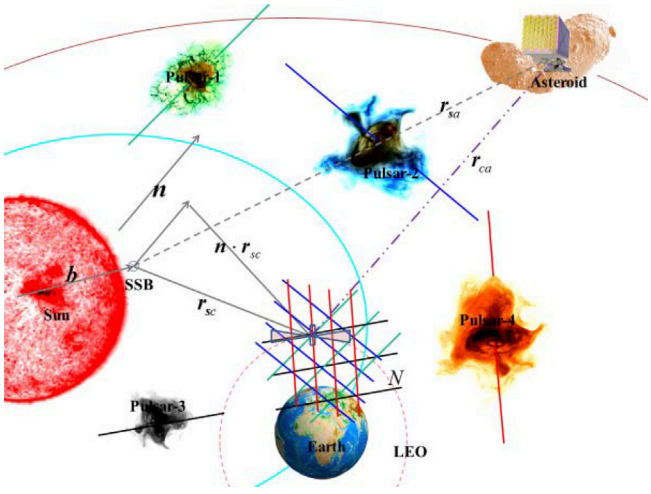


**Fig. 11.** The XNAV astronomical observatory. The ranging between LEO satellite (such as ISS) and asteroid (XNAV detector onboard) measured by XNAV could reflect comprehensive information beneficial to astrophysics and planetary geodesy. The mathematical model can be deduced from XNAV relative navigation.

#### 4.2.2. OCN observations for planetary sciences

The OCN system has been realized in approaching phase of Mars orbit, which provides another navigation independent on the ground tracking system. The technique will be the main autonomous method for Mars spacecraft before the XNAV achieve high accuracy as a few kilometers. The navigational sensors, e.g., cameras, which would be integrated into two-in-one combination to complete the scientific goals are expected. The star Light Occultation observations could help acquiring atmospheric refraction information, which can be used in Mars orbiting navigation and atmospheric parameters retrieve.

The integration of the above XNAV, OCN, GAO and other navigational forms is beneficial in both navigation engineering and scientific exploration for deep space missions. The combination, which use star sensor to keep the attitude and adopt XNAV as positioning and navigation solutions realized in SEXTANT (Winternitz et al., 2016), will be one of the deep-space navigation trends of the future missions. The passive navigation and its integrated forms may show its power in this field.

## 5. Conclusion

The XNAV system can provide autonomous navigation solutions for Mars Missions, which the accuracy can achieve 300–500 m by observing three X-ray Pulsars PSR B1937 + 21, B1821–24 and B0531 + 21. The increasing of the numbers of the observed Pulsars can improve the accuracy, however, which would also bring observed burdens to the system. The geometric distribution of the Pulsars has major influence on the performance of XNAV. The signal switchover among Pulsars will cause accuracy fluctuations to the system, which can be steadied by integrating OCN to the system. The OCN system has lower accuracy but stable performance, which is a practical navigation method for current Mars missions. The GAO could be another autonomous absolute positioning solution to the Mars rovers, which is currently tracked by ground radio beams. The TERCOM algorithm is more suitable for the GAO system.

The precise observations achieved by these systems can also promote interplanetary scientific research in terms of Planetary Geodesy and Astrophysics (PGA). Particularly, accurate POD results of XNAV achieved by appropriate 3 or 4 Pulsars combinations have vast prospective in estimating scientific parameters which are important for PGA.

## Acknowledgement

The research is supported by National Basic Research Program of China (973 Program) (Grant No. 2012CB72000).

## Appendix E. Supplementary data

Supplementary data related to this article can be found at https://doi.org/10.1016/j.pss.2018.06.014.

## Appendix

### Appendix A. XNAV algorithms

#### Appendix A.1. Time transfer from local to reference scale

The periodic pulses emitted from a rotation-powered milliseconds X-ray pulsar can be collected by optics and detected by detector onboard the spacecraft. The detector is required to have individual X-ray photo detection capability. Once the photo was received, it will be stamped with time tag by the atomic clock with uncertainties less than 1 μs (Okajima et al., 2016). The clock onboard a spacecraft is commonly modulated with UTC scales, synonymously, TT scales:

$$TT = UTC + \Delta TT \tag{A.1}$$

The $\Delta TT$ is a constant includes leap seconds. The TT can be transferred to TCG by adding a long-term drift to the TT:

$$TCG = TT + L_G \times (JD_{TT} - TT_0) \tag{A.2}$$

The $L_G$ is the geocentric drift constant. $JD_{TT}$ is the TT time expressed in the format of Julian Day. $TT_0$ is the beginning of the TT. The TCB can be obtained from TCG by using the orbit information of the spacecraft and dynamical ephemeris such as DE series:

$$TCB - TCG = c^2 \left\{ \int_{t_0}^{t} \left[ \frac{v_e^2}{2} + U_{ext}(\mathbf{x_e}) \right] dt + \mathbf{v_e} \bullet (\mathbf{x} - \mathbf{x_e}) \right\} + O(c^{-4}) \tag{A.3}$$

The $\mathbf{x_e}$ and $\mathbf{v_e}$ is the position and velocity in Geocentric Inertial Coordinate System. $c$ is the speed of light. $U_{ext}$ is the sum of gravitational potential of the solar system. The TCB also can be further transferred to TDB to apply in practical cases:

$$TDB = TCB - L_B(JD_{TCB} - T_0) \times 86400 + TDB_0 \tag{A.4}$$

The transfer of time among different scales has been investigated by International Astronomy Union (IAU). We use IAU SOFA packages (In FORTRAN 77) to transfer the time scale. The process how to tag the arrival X-ray photos and to estimate the parameters are described in Winternitz et al. (2015).

#### Appendix A.2. Phase Doppler Locking Loop(PDLL) Algorithm

The vehicles' moving along or away from the Pulsar in light-of-sight would cause Doppler Effect in the detected signal phase. The phase detected on moving vehicles can be described with neglected high order terms as follows (Golshan and Sheikh, 2007; Anderson et al., 2015):

$$\phi_{\text{det}} = \phi_0 + f_P(t - t_0) + \frac{f_P}{c} \int_{t_0}^{t} v(\tau) d\tau \tag{A.5}$$

The $\phi_{\text{det}}$ is the detected phase acquired by the onboard detector. The $\phi_0$ is the initial phase. The $t$ is epoch and $t_0$ is reference time. $f_P$ is the rotation frequency of the Pulsars. $v$ is velocity of the spacecraft along in the Line-of-Sight of the Pulsar. The Doppler Effect can be estimated by using the prior

orbit information provided by orbit dynamical model. Two cases can be seen from Anderson et al. (2015) and Wang and Zhang (2016). The estimation can be inducted in the local time scale (A.1) or reference time scale (A.3) & (A.4). The pulse of the latter is more distinguished, but the time transfer process would cause phase errors due to use the prior orbit information (Winternitz et al., 2016). The parameters fixing of the processes are based on the Non-Homogeneous Poisson Distribution (NHPD) of photons received within fixed time intervals (Winternitz et al., 2016).

*Appendix A.3. Absolute Navigation Algorithm.*

The period beacons eject from an X-ray Pulsar has predictable phase, which can be modeled in the origin of the inertial coordinate system such as Solar System Barycenter (SSB) by long term observations. The template phase has similar form as (A.5), which includes high order terms (Wang and Zhang, 2016):

$$\phi(t) = \phi(t_0) + f_P(t - t_0) + \frac{\dot{f}_P}{2}(t - t_0)^2 + \frac{\ddot{f}_P}{6}(t - t_0)^3 \tag{A.6}$$

The template phase can be built with reference time scale. The process includes transfer local time measured by an atom clock to an initial origin, e.g., SSB as described in Appendix A.1. The accurate solution to equations (A.3) and (A.4) can be achieved by boarding Global Navigation Satellite System (GNSS) receiver and XNAV optics and detector simultaneously in a Low Earth Orbit (LEO) satellite. The LEO satellite orbit determined by GNSS techniques could achieve high accuracy. As well as, high accuracy dynamical ephemeris of the celestial bodies within solar system is also needed to obtain the $U_{ext}$.

To compare the X-ray flux signal Time Of Arrive (TOA) to the spacecraft with template or predicted Time of Arrive, the TOA to the probe has to be transfer to the same reference origin SSB by using transfer algorithm illustrated in Appendix A.1. The difference of the barycentric TOA of the spacecraft and the template TOA can be expressed as follows:

$$c(t_{ssb} - t_{sc}) = cP(\Delta\phi + N) \tag{A.7}$$

Here, $t_{ssb}$ is the predicted TOA by models in SSB. $t_{sc}$ is the barycentric observed TOA. $P$ represents the period of the Pulsar. $\Delta\phi$ is the phase shift between measured signal and predicted signal; N is ambiguity of the phase. The observation equation of the absolute navigation is as follows (Sheikh et al., 2006; Shemar et al., 2016):

$$\begin{cases} t_{ssb} - t_{sc} = \dfrac{1}{c}\mathbf{n}\cdot\mathbf{r_{ps}} + \delta t_{roemer} + \delta t_{shapiro} + \delta t_c + v_\tau \\ \delta t_{reomer} = \dfrac{1}{2cD_0}\left[(\mathbf{n}\cdot\mathbf{r_{ps}})^2 - r_{ps}^2 + 2(\mathbf{n}\cdot\mathbf{b})(\mathbf{n}\cdot\mathbf{r}_{ps}) - 2(\mathbf{b}\cdot\mathbf{r}_{ps})\right] \\ \delta t_{shapiro} = \dfrac{2\mu_s}{c^3}\ln\left|\dfrac{\mathbf{n}\cdot\mathbf{r}_{ps} + \mathbf{n}\cdot\mathbf{b} + \|\mathbf{r}_{ps} + \mathbf{b}\|}{\mathbf{n}\cdot\mathbf{b} + b}\right| \\ \delta t_c = a_0 + a_1(t - t_0) \end{cases} \tag{A.8}$$

The details of the derivation of this equation were issued in documents (Sheikh et al., 2006). The meanings of the symbols are listed in Table A1.

**Table A.1**
A symbols list of equation (A.7).

| | | | |
|---|---|---|---|
| $c$ | the speed of light | $\mathbf{n}$ | the direction vector of the Pulsar |
| $\mathbf{r_{sp}}$ | position vector of the probe | $\mathbf{b}$ | position vector of sun |
| $\delta t_{romer}$ | the Roemer delay (part) | $a_0$ | the clock offset |
| $\delta t_{shapiro}$ | the Shapiro delay | $a_1$ | the clock drift |
| $v_\tau$ | random noise | $\delta t_c$ | clock uncertainties |
| $D_0$ | the initial position of Pulsars | $\mu_s$ | the heliocentric gravitational constant |

*Appendix A.4. Delta Correction Algorithm.*

Traditionally, the trajectory of a spacecraft can be predicted by an orbit propagator using the dynamical equations. The estimated or predicted orbit by the dynamical equations has errors compared with the true position, which is as follows:

$$\delta\mathbf{r_{sp}} = \mathbf{r_{sp}} - \widehat{\mathbf{r}}_{\mathbf{sp}} \tag{A.9}$$

$\delta\mathbf{r_{sp}}$ represents the correction between true and predicted orbit. $\widehat{\mathbf{r}}_{\mathbf{sp}}$ represent the orbit vector estimated by dynamical propagator. The pulse TOA to the reference origin such as SSB can be predicted by using the predicted orbit information and related celestial ephemeris transfer and model. This estimated TOA $\widehat{t}_{ssb}$of the template reference would have errors if the model was built by true orbit of the probe and true position of the celestial bodies:

$$\delta t_{ssb} = t_{ssb} - \widehat{t}_{ssb} \tag{A.10}$$

As well as, the estimated TOA to the spacecraft $\widehat{t}_{sc}$ has difference with the true TOA $t_{sc}$:

$$\delta t_{sc} = t_{sc} - \widehat{t}_{sc} \tag{A.11}$$

The delta-correction method uses these corrections to construct the observation equations by inserting (A.10) and (A.11) into (A.8) to shape a form as:

$$\delta t_{ssb} = \delta t_{sc} + \mathbf{A} \bullet \delta\mathbf{r}_{sp} \tag{A.12}$$

The terms of design matrix **A** is described in (Sheikh et al., 2006). (A.12) is the observation equation of the Delta Correction method.

*Appendix A.5. The ranging accuracy evaluated by hardware parameters and features of pulsars.*

The ranging accuracy can be evaluated by multiplying the speed of light to the pulse TOA errors which acquired from the hardware parameters and statistic frequency information such as Signal-Noise-Ratio (SNR). The ranging error is as follows (Sheikh et al., 2006; Shemar et al., 2016):

$$\sigma_L = 0.5KcW_{50}P\frac{\sqrt{1+\left(F_{bX}\Omega_{efc}+F_{bN}A_{\mathrm{det}}/A_{efc}\right)/f_pF_{total}}}{X_p\sqrt{A_{efc}T_{obs}f_pF_{total}}} \tag{A.13}$$

The $\sigma_L$ is the ranging errors which independent with the rang between spacecraft and SSB. The $K$ is the weighting factor of SNR, which the value is between 0.5 and 1. The $W_{50}$ is the characteristic width of the Pulsars. $c$ is speed of light and $P$ is the Rotation period of the Pulsar. $F_{bX}$ is the background X-ray Flux duo to diffusing from sky, which approximates 5 ph $cm^{-2}$ $s^{-1}$ $sr^{-1}$. $F_{bN}$ represents other X-ray Fluxes noise such as cosmic background and detector noise, which is about 0.1 ph $cm^{-2}$ $s^{-1}$. $\Omega_{\mathrm{efc}}$ is the source-detection solid angle, which sets to 0.033 sr in the paper. $A_{\mathrm{det}}$ is the area of the detector and $A_{\mathrm{efc}}$ is the effective area. $f_p$ equals to 1/P. $F_{total}$ is the Flux from the navigational Pulsars. $X_p$ is the pulse power. $T_{\mathrm{obs}}$ is the observation duration. The parameters of seven X-ray Pulsars are listed in Table A2. The evaluating results of the Pulsars are listed in Table A3.

**Table A.2**
The parameters of the seven X-ray Pulsars and its position in Right Ascension and Declination.

| Parameters PSR | Period/s | Total Flux/ph $cm^{-2}$ $s^{-1}$ | $W_{50}$ | Pulse power | Position Error/mas | RA/deg | DEC/deg |
|---|---|---|---|---|---|---|---|
| B1937 + 21 | 0.00155 | 1.40 | 0.02 | 0.86 | 0.04 | 294.91067 | 21.58309 |
| B1821-24 | 0.00305 | 0.52 | 0.03 | 0.98 | 6.01 | 276.13340 | −24.86960 |
| B0531 + 21 | 0.03308 | 3200.00 | 0.05 | 0.70 | 3.43 | 83.63322 | 22.01446 |
| B0540-69 | 0.05035 | 160.00 | 0.45 | 0.67 | 69.07 | 85.04667 | −69.33171 |
| J0218 + 4232 | 0.00232 | 2.20 | 0.11 | 0.73 | 31.12 | 34.52649 | 42.53816 |
| J0205 + 6449 | 0.06568 | 61.00 | 0.03 | 0.20 | 714.49 | 31.40801 | 64.82815 |
| J0437-4715 | 0.00575 | 4.400 | 0.30 | 0.37 | 0.05 | 69.31623 | −47.25253 |

**Table A.3**
The ranging errors(*km*) estimated by equation (A.13).

| PSR $T_{obs}(s)$ | B1937 + 21 | B1821-24 | B0531 + 21 | B0540-69 | J0218 + 4232 | J0205 + 6449 | J0437-4715 |
|---|---|---|---|---|---|---|---|
| | $A_{\mathrm{det}} = 0.6\ m^2$ $A_{\mathrm{efc}} = 0.5\ m^2$ | | | | | | |
| 600 | 0.0058 | 0.0388 | 0.0358 | 2.8496 | 0.0550 | 1.5674 | 0.8221 |
| 1200 | 0.0041 | 0.0274 | 0.0253 | 2.0150 | 0.0389 | 1.1083 | 0.5813 |
| 1800 | 0.0034 | 0.0224 | 0.0207 | 1.6452 | 0.0318 | 0.9050 | 0.4746 |
| 2400 | 0.0029 | 0.0194 | 0.0179 | 1.4248 | 0.0275 | 0.7837 | 0.4111 |
| 3000 | 0.0026 | 0.0174 | 0.0160 | 1.2744 | 0.0246 | 0.7010 | 0.3677 |
| 3600 | 0.0024 | 0.0158 | 0.0146 | 1.1633 | 0.0225 | 0.6399 | 0.3356 |

**Table A.4**
The combined X-ray Pulsars groups.

| Group / PSR | *T-a* | *T-b* | *T-c* | *T-d* | *F-a* | *F-b* | *S-a* |
|---|---|---|---|---|---|---|---|
| B1937+21 | √ | | | | √ | | √ |
| B1821-24 | √ | √ | | √ | √ | | √ |
| B0531+21 | √ | | | | √ | | √ |
| B0540-69 | | | √ | √ | | √ | √ |
| J0218+4232 | | √ | | √ | √ | √ | √ |
| J0205+6449 | | | √ | | | √ | √ |
| J0437-4715 | | √ | √ | | | √ | √ |

To classify the Pulsars into several groups based on the ranging errors are illustrated in Table A4 we have separated the Pulsars into groups which are recapitulative combinations in terms of high, medium, and low accuracy. More combinations can be realized in 3 and 4 Pulsars groups. However, the groups in Table A4 are the most representative.

*Appendix A.6. The Results of the combinations XNAV.*

The XNAV results for Mars spacecraft are listed from Figure A.1 to Figure A.5, which include position and velocity errors from combination *T-b, T-d, F-a, F-b,* and *S-a* as shown in Table A4. For *T-b* and *T-d*, the velocity errors are within 3 m/s, which likes the combination *T-a*. The position accuracy of *T-d* shows the appropriate arranging of the navigational Pulsars can improved the performance of XNAV tremendously compared with *T-c* shown in Fig. 4. The increasing in the number of Pulsars cannot improve the accuracy largely but it can make XNAV achieving higher accuracy navigation results in a very stable way. *F-a*, *F-b*, and *S-a* are good examples. The worst case of 4-Pulsars combination (*F-b*) achieves 3 km and 15 m/s position and velocity accuracy, respectively. For *S*-a, e.g., the 7-Pulsars combination, which includes all kinds of Pulsars, has similar accuracy performance with *T-a* and *F-a*. Therefore, the scanned targets of XNAV have major influence on the performance of the system.

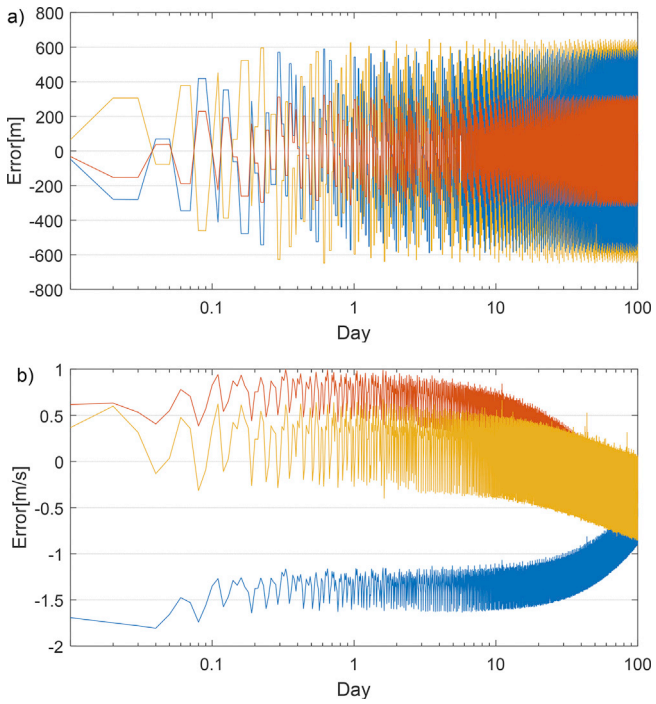


**Fig. A.1.** Orbit accuracy determined by B1821–24, J0218 + 4232 and J0437–4715.

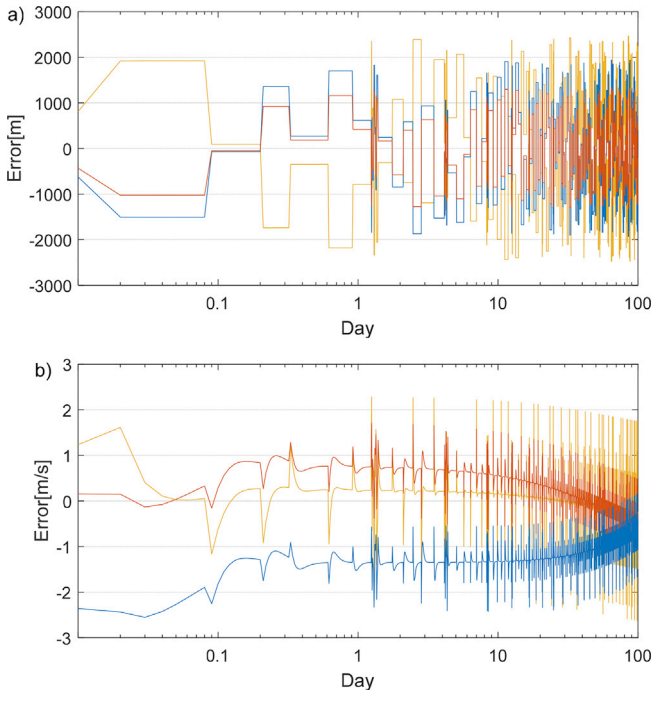


**Fig. A.2.** Orbit accuracy determined by B1821–24, B0540–B0569 and J0218 + 4232.

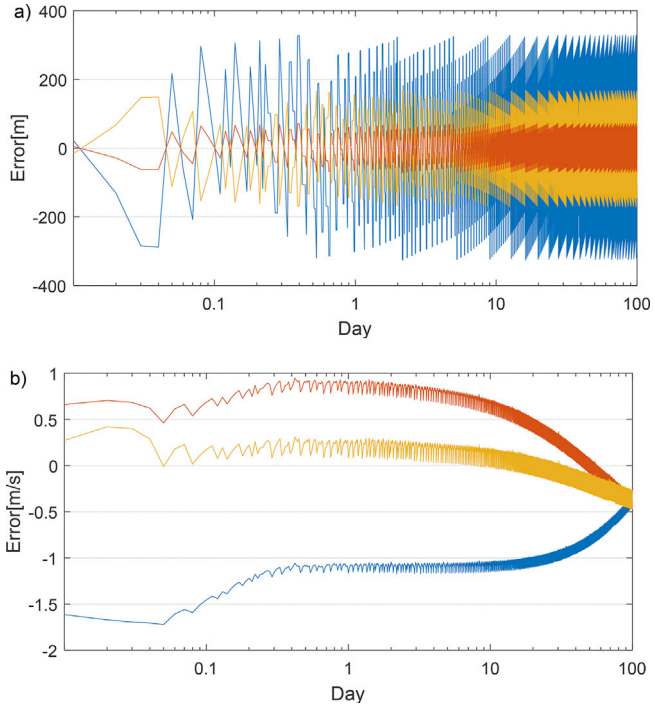


**Fig. A.3.** Orbit accuracy determined by B1937 + 21, B1821–24, B0531 + 21 and J0218 + 4232.

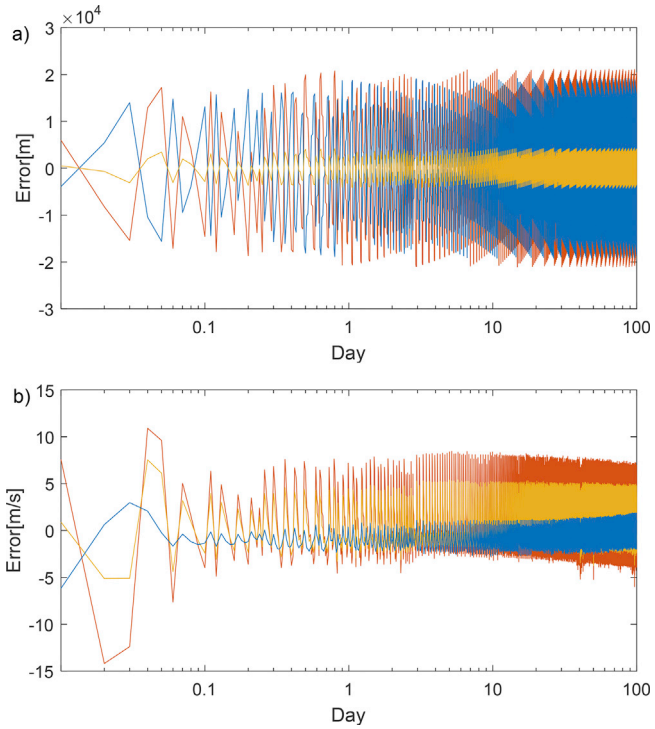


**Fig. A.4.** Orbit accuracy determined by B0540–69, J0218 + 4232, J0205 + 6449 and J0437–4715.

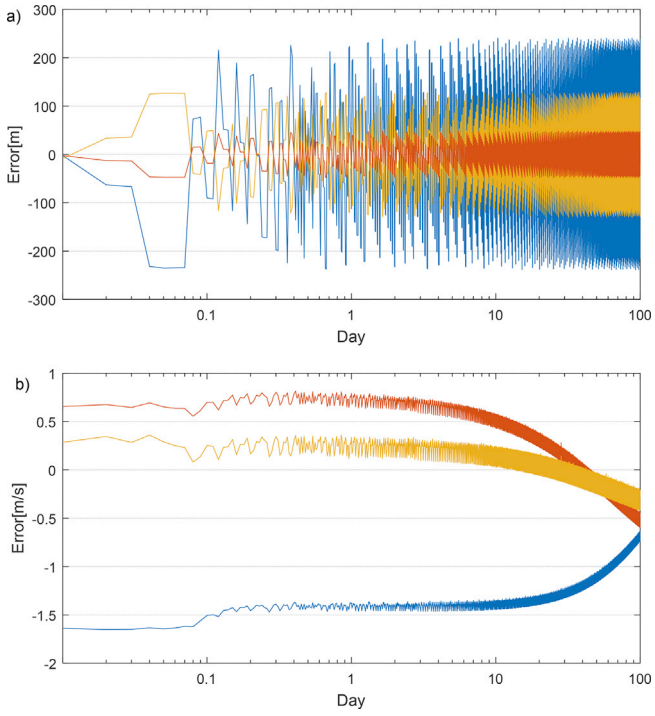


**Fig. A.5.** Orbit accuracy determined by seven pulsars as shown in Table A5.

**Table A.5**
The orbital accuracy determined by 7-Pulsars combinations.

| | 7-Pulsars of this paper | | | | 7-Pulsar from Liu et al. (2017) | | | |
|---|---|---|---|---|---|---|---|---|
| | $a_0 = 10^{-9}s$ | | $a_1 = 10^{-10}s$ | | $T = 864$ s | | $A = 0.5$ m$^2$ | |
| | max | min | mean | SD | max | min | mean | SD |
| X | 240.8 | −238.8 | 0.9 | 137.9 | 21.46 km | −14.97 km | −31.4 | 2.35 km |
| Y | 48.5 | −48.1 | 0.1 | 27.8 | 729.7 | −552.6 0.8104.3 | | |
| Z | 128.8 | −130.2 | −0.68 | 74.4 | 3.94 km | −6.20 km | 6.5 | 690.2 |
| VX | −0.63 | −1.65 | −1.09 | 0.23 | −0.15 | −30.81 | −17.62 | 2.56 |
| VY | 0.82 | −0.60 | −0.03 | 0.36 | 0.78 | −28.36 | −16.43 | 2.24 |
| VZ | 0.36 | −0.42 | −0.08 | 0.17 | 0.12 | −30.19 | −16.29 | 2.24 |

Table A5 shows the navigation results of XNAV by different 7-Pulsars combinations. We use Equation (A.13) to evaluate frequently used navigational Pulsars by other researches to select the most suitable targets for XNAV. The selected Pulsars have better navigation performance than the combination described in Liu et al. (2017). The combination in this paper achieves 250 m and 2 m/s navigation accuracy, which is also illustrated in Figure A.5.

*Appendix B. OCN algorithm and simulated results.*

*Appendix B.1. The observational equation of the OCN techniques.*

The star light comes into a star tracker or camera is first filtered, reflected, and projected into the detector plain (CCD or other sensors). The image collected by the detector is transferred into digital signal by external circuit. Then, the signal processing system transfers the signal into observations such as Light-in-Sight or Angles between celestial bodies. The transfer process includes star recognizing, tracking, and extracting the center of the bodies. We use angles as observations in terms of Sun-sc-Sirius, Sun-sc-Earth, Sun-sc-Mars, and Earth-sc-Mars. The angles or angles distance observations have relationship with Light-in-Sight measurements as follows (Liu et al., 2017):

$$\zeta = \arccos(l_1, l_2) + v_\zeta \tag{B.1}$$

$\zeta$ is the angle. $l_1$ and $l_2$ are celestial bodies Light-in-Sight measured by the camera onboard the spacecraft. The $l$ is a constant if the body is star. The $l$ is as follows for nearby bodies:

$$\mathbf{l} = \frac{\mathbf{r_{cb}} - \mathbf{r}_{sp}}{\left|\mathbf{r_{cb}} - \mathbf{r}_{sp}\right|} \tag{B.2}$$

The position of celestial bodies $\mathbf{r_{cb}}$ can be acquired from numeric ephemeris such as DE series.

*Appendix B.2. The simulation results of integrated XNAV and OCN system.*

Part of the results of the integrated XNAV and OCN system are portrayed in Figure B.1 and Figure B.2. As discussed in section 3.2.2, the performance

of the OCN approximates 300 km and 15 m/s in terms of position and velocity errors. The integrated system dose has velocity improvement compared Figure B.2 with Figure A.2. Indeed, the XNAV influences the errors SD by different combinations but the mean value of the errors keeps the same due to the main influence of the integrated system is controlled by OCN subsystem in the paper. The performance of the OCN system is stable which is indicated by comparing Figure B.1, Figure B.2, and Figures in section 3.2.

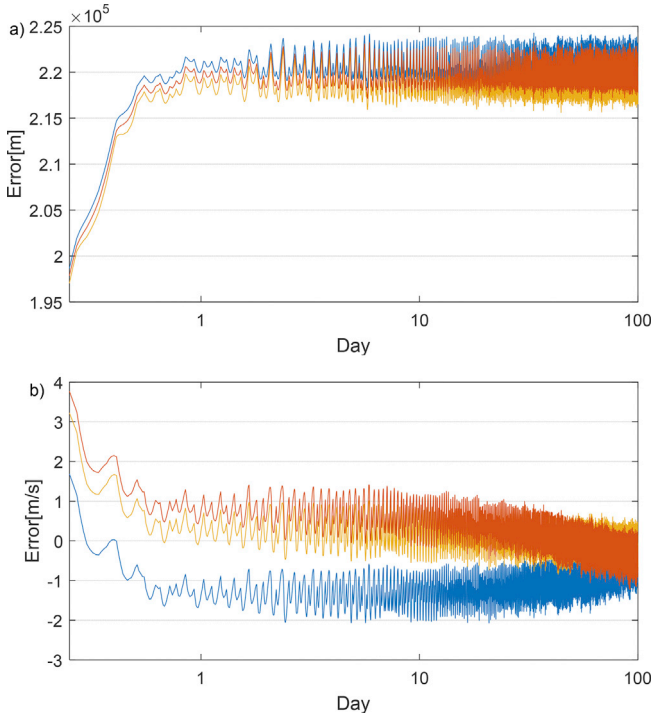


**Fig. B.1.** . Navigation performance of integrated XNAV and OCN (T-b/OCN).

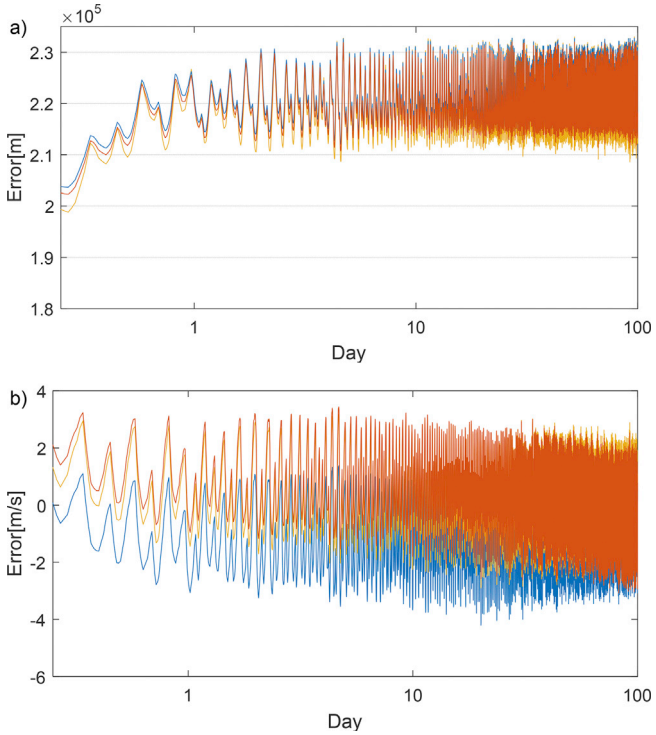


**Fig. B.2.** . Navigation performance of integrated XNAV and OCN (T-d/OCN).

## Appendix C. The matching method of the Gravity-aided odometry.

### Appendix C.1. The Iterated Closest Point Algorithm.

The initial trajectories of rovers are provided by celestial heading and dead-reckoning by wheel coding. The Vision odometry can also provide high accuracy relative trajectories by tracking homonymy points of image pairs. The position of first several initial points is solved by ground-based or orbiter-rovers radio tracking techniques. The Iterated Closest Point Algorithm for GAO is to find the closest point in the background map based on the initial trajectory $\rho = [B, L]^T$ and gravity anomaly measurements $g$. The simulated trajectory and observations are as follows:

$$\begin{cases} \rho(i)_{\text{sim}} = \rho(i) + i \times rnd \times 0.017^{\circ}/3600 + rnd \times 0.002^{\circ} \\ g_{sim} = g + 2\text{m}Gal \times rnd + 0.01mGal \times rnd \end{cases} \tag{C.1}$$

Wherein, $B$ is longitude and $L$ represents latitude; $i$ is the points numbers along the trajectory. The long-term drift and random noises are added to the $\rho$ to generate the simulated trajectory $\rho_{sim}$. The uncertainties (2 mGal random values) between the observations and the map values are mixed into the true gravity anomalies $g$. The observation errors of the instrument are also added to. The core idea of the ICP is to fix the rotation and shift relationship in terms of rotation $R$ and shift matrix $T$ between the simulated values $x$ in Equation (C.1) and the closest values $\hat{x}$ in the background map by iterated loop:

$$\hat{x}\left(\rho_{icp}, \text{g}_{\text{icp}}\right) = R \bullet x(\rho_{sim}, \text{g}_{\text{sim}}) - T \tag{C.2}$$

When the $|\hat{x} - x| < \tau$, the iteration will end. $\tau$ is the threshold.

### Appendix C.2. Terrain Contour Matching.

The TERCOM algorithm is implemented to fulfill the Equation (1) by searching the field around the initial trajectory $\rho$. The Monte Carlo method is used to generate searching trajectories which keep same shape with the simulated traverse but shifted by fixed intervals in the directions of longitude and latitude. The interval equals to 1″ and the searching scope is 3′. Therefore, the number of the searching trajectories $n$ equals to $180 \times 180$. The optimal trajectory is the one which fulfill the criteria that could minimize the equation as follows:

$$\sigma = \frac{1}{m}\sum_{k=1}^{m}\left[(g_{search} - g_{\text{sim}})^2 + (B_{search} - B_{sim})^2 + (L_{search} - L_{sim})^2\right] \tag{C.3}$$

Where σ is the criteria function. $m$ is the number of traverse points of the initial trajectory.

## Appendix D. Kalman Filter used in this simulation.

### Appendix D.1. Unscented Kalman Filter.

The Cruise orbit of Mars spacecraft can be predicted by dynamical model. We use dynamical model to model the motion of the probe:

$$\mathbf{a} = -\frac{\mu_s}{r_{ps}^3}\mathbf{r}_{ps} - \mathbf{a}_m - \mathbf{a}_e + \mathbf{w}_\mathbf{a} \tag{D.1}$$

The $\mathbf{a}_m$ and $\mathbf{a}_e$ are gravitational perturbations caused by Mars and Earth, respectively. $\mathbf{w}_\mathbf{a}$ is model noises. Runge-Kutta 8 (7) integrator is used to solve the differential equation (D.1). The solution is regarded as the fist-step prediction of the Unscented Kalman Filter (UKF). The sigma points and its weight of the UKF are generated by symmetric sampling based on the solution $\overline{X}$:

$$\begin{aligned} &S_0 = \overline{X}; W_0^{\text{m}} = \lambda/(n+\lambda), W_0^{\text{c}} = [\lambda/(n+\lambda)] + \left(1 + \alpha^2 + \beta\right) \\ &S_i = \overline{X} + \gamma\left(\sqrt{P_{xx}}\right)_i, 0 < i \le n; \quad W_i^{\text{m}} = W_i^{\text{c}} = \lambda/2(n+\lambda) \\ &S_i = \overline{X} - \gamma\left(\sqrt{P_{xx}}\right)_i, n < i \le 2n \end{aligned} \tag{D.2}$$

The $\overline{X}$ is a $6 \times 1$ vector including position and velocity of the probe, that is, $\text{n} = 6$. $\gamma = \sqrt{n + \lambda}$ and $\lambda = \alpha^2(n + \kappa) - n$. The parameter$\alpha$, $\beta$and$\kappa$ can be set based on the practical situation of Kalman filter. $\left(\sqrt{P_{xx}}\right)_i$ represents the $i$-th row of the upper triangular matrix decomposed from matrix of first-step predicted errors by the Cholesky decomposition. The details of update the UKF is illustrated in (Kandepu et al., 2008).

### Appendix.D.2. Federal Kalman Filter.

The solution of the Federal Kalman Filter is acquired by using the weighted average values from subsystems. The integrated XNAV and OCT system is solved by ($t$=$k$):

$$\begin{cases} \hat{X}_{INT}(k) = P_{INT}(k) \cdot \left[P_{XNAV}^{-1}(k)X_{XNAV}(k) + P_{OCT}^{-1}(k)X_{OCT}(k)\right] \\ P_{INT}(k) = \left[P_{XNAV}^{-1}(k) + P_{OCT}^{-1}(k)\right]^{-1} \end{cases} \tag{D.3}$$

The subsystem XNAV and OCN are simulated by UKF using observational equation (A.8) and (B.1), respectively. The integrated results $\hat{X}_{INT}(k)$ and its variance $P_{INT}(k)$ are returned as initial input for the first-step prediction of the subsystem for $t$=$k$+1 epoch. The feedback process is adjusted in term of information fusion factor as follows:

$$\beta_j = \frac{\left\|P_j(k)\right\|^{-1}}{\sum_{j=1}^{2}\left\|P_j(k)\right\|^{-1}} \tag{D.4}$$

Where $j$=XNAV, OCN. $\left\|P_j(k)\right\| = \sqrt{\sum diag(P_j^T(k) \cdot P_j(k))}$. The evaluation of the FKF are illustrated in Carlson (1990).

## References


Anderson, K.D., Pines, D.J., Sheikh, S.I., 2015. Validation of pulsar phase tracking for spacecraft navigation. J. Guid. Contr. Dynam. 38 (10), 1–13. https://doi.org/10.2514/1.G000789.

Becker, W., Bernhardt, M.G., Jessner, A., 2013. Autonomous spacecraft navigation with pulsars. Acta Futura 7, 11–28. https://doi.org/10.2420/AF07.2013.11.

Becker, W., Kramer, M., Sesana, A., 2018. Pulsar timing and its application for navigation and gravitational wave detection. Space Sci. Rev. 214 (30), 10.1007/s11214-017-0459-0.

Carlson, N.A., 1990. Federated square root filter for decentralized parallel processors. IEEE Trans. Aero. Electron. Syst. 26 (3), 517–525. https://doi.org/10.1109/7.106130.

Centinello III, F.J., Zuber, M.T., Smith, D.E., Mazarico, E., 2015. Orbit determination of the dawn spacecraft with radiometric and image data. J. Spacecraft Rockets 52 (5), 1331–1337. https://doi.org/10.2514/1.A33224.

Chester, T.J., Butman, S.A., 1981. Navigation using X-ray pulsars. In: NASA Technique Report 81N27129, pp. 22–25. https://tmo.jpl.nasa.gov/progress_report/42-63/63F.PDF.

Downs, G.S., 1974. Interplanetary navigation using pulsating radio sources. In: NASA Technique Report 74N34150, pp. 1–10. https://ntrs.nasa.gov/archive/nasa/casi.ntrs.nasa.gov/19740026037. pdf.

Guinn, J.R., Riedel, J.E., Bhaskaran, S., Park, R.S., Vaughan, A.T., Owen, W.M., Martin-Mur, T.J., 2016. The deep-space positioning system concept: automating complex navigation operations beyond the earth. In: AIAA SPACE 2016 (5409), 1–18. https://doi.org/10.2514/6.2016-5409.

Golshan, A.R., Sheikh, S.I., 2007. On pulse phase estimation and tracking of variable celestial X-ray sources. In: Institute of Navigation 63rd Annual Meeting, pp. 413–422.

Hirt, C., Claessens, S.J., Kuhn, M., Featherstone, W.E., 2012. Kilometer-resolution gravity field of mars: mgm2011. Planet. Space Sci. 67 (1), 147–154. https://doi.org/10.1016/j.pss.2012.02.006.

Jin, S.G., Arivazhagan, S., Araki, H., 2013. New results and questions of lunar exploration from SELENE, Chang'E-1, Chandrayaan-1 and LRO/LCROSS. Adv. Space Res. 52 (2), 285–305. https://doi.org/10.1016/j.asr.2012.11.022.

Jin, S.G., Zhang, T.Y., 2014. Automatic detection of impact craters on Mars using a modified adaboosting method. Planet. Space Sci. 99, 112–117. https://doi.org/10.1016/j.pss.2014.04.021.

Jircitano, A., White, J., Dosch, D., 1990. Gravity based navigation of auvs. In: Autonomous Underwater Vehicle Technology 1990 IEEE, pp. 177–180. https://doi.org/10.1109/AUV.1990.110453.

Jircitano, A., Dosch, D.E., 1991. Gravity aided inertial navigation system (GAINS). In: Institute of Navigation, 47th Annual Meeting, vol. 1, pp. 221–229.

Kandepu, R., Foss, B., Imsland, L., 2008. Applying the unscented kalman filter for nonlinear state estimation. J. Process Contr. 18 (7–8), 753–768. https://doi.org/10.1016/j.jprocont.2007.11.004.

Karimi, R.R., Mortari, D., 2015. Interplanetary autonomous navigation using visible planets. J. Guid. Contr. Dynam. 38 (6), 1151–1156. https://doi.org/10.2514/1.G000575.

Liebe, C.C., 2002. Accuracy performance of star trackers - a tutorial. IEEE Trans. Aero. Electron. Syst. 38 (2), 587–599. https://doi.org/10.1109/TAES.2002.1008988.

Liebe, C.C., Murphy, N., Dorsky, L., Udomkesmalee, N., 2016. Three-axis sun sensor for attitude determination. IEEE Aero. Electron. Syst. Mag. 31 (6), 6–11. https://doi.org/10.1109/MAES.2016.150024.

Liu, J., Wei, E., Jin, S., 2017. Mars cruise orbit determination from combined optical celestial techniques and x-ray pulsars. J. Navig. 70 (4), 719–734. https://doi.org/10.1017/S0373463316000874.

Liu, J., Wei, E., Jin, S., 2018. Absolute navigation and positioning of mars rover using gravity-aided odometry. J. Navig. 1–17. https://doi.org/10.1017/S0373463317000893.

Maimone, M., Johnson, A., Cheng, Y., Willson, R., Matthies, L., 2006. Autonomous navigation results from the mars exploration rover (MER) mission. Exp.Robot. 21, 3–13. https://doi.org/10.1007/11552246_1.

Martinmur, T.J., Kruizinga, G.L., Burkhart, P.D., Abilleira, F., Wong, M.C., Kangas, J.A., 2011. Mars science laboratory interplanetary navigation. J. Spacecraft Rockets 51 (4), 1014–1028. https://doi.org/10.2514/1.A32631.

Mortari, D., Conway, D., 2017. Single-point position estimation in interplanetary trajectories using star trackers. Celestial Mech. Dyn. Astron. 128 (1), 115–130. https://doi.org/10.1007/s10569-016-9738-4.

Mitchell, J.W., Hassouneh, M.A., Winternitz, L.M., Valdez, J.E., Price, S.R., Semper, S.R., Litchford, R.J., 2015. SEXTANT—station explorer for X-ray timing and navigation technology. In: AIAA Guidance, Navigation, and Control Conference, 2015–0865.

Okajima, T., Soong, Y., Balsamo, E., Enoto, T., Olsen, L., Koenecke, R., Kenyon, S., 2016. Performance of NICER flight x-ray concentrator. In: SPIE Astronomical Telescopes& Instrumentation, vol. 9905. https://doi.org/10.1117/12.2234436 (99054X), 1–7.

Prigozhina, G., Gendreaub, K., Fostera, R., Rickera, G., Villasenora, J., Dotyd, J., Huberc, A., 2012. Characterization of the silicon drift detector for NICER instrument. In: Proceedings of SPIE, vol. 8453. https://doi.org/10.1117/12.926667 (845318), 1–7.

Reichley, P., Downs, G., Morris, G., 1971. Use of pulsar signals as clocks. JPL Q. Tech. Rev. 1 (1), 80–86.

Rice, H., Mendelsohn, L., Aarons, R., Mazzola, D., 2000. Next generation marine precision navigation system. In: Position Location and Navigation Symposium IEEE, vol. 2000, pp. 200–206. https://doi.org/10.1109/PLANS.2000.838303.

Shemar, S., Fraser, G., Heil, L., Hindley, D., Martindale, A., Molyneux, P., et al., 2016. Towards practical autonomous deep-space navigation using x-ray pulsar timing. Exp. Astron. 42 (2), 101–138. https://doi.org/10.1007/s10686-016-9496-z.

Sheikh, S.I., Pines, D.J., Wood, K.S., Ray, P.S., Lovellette, M.N., Wolff, M.T., 2006. Spacecraft navigation using x-ray pulsars. J. Guid. Contr. Dynam. 29 (1), 49–63. https://doi.org/10.2514/1.13331.

Wang, H., Wu, L., Chai, H., Hsu, H., Wang, Y., 2016a. Technology of gravity aided inertial navigation system and its trial in South China Sea. IET Radar, Sonar Navig. 10 (5), 862–869. https://doi.org/10.1049/iet-rsn.2014.0419.

Wang, B., Yu, L., Deng, Z., Fu, M., 2016b. A particle filter-based matching algorithm with gravity sample vector for underwater gravity aided navigation. IEEE ASME Trans. Mechatron. 21 (3), 1399–1408. https://doi.org/10.1109/TMECH.2016.2519925.

Wang, Y., Zhang, W., 2016. Pulsar phase and Doppler frequency estimation for XNAV using on-orbit epoch folding. IEEE Trans. Aero. Electron. Syst. 52 (5), 2210–2219. https://doi.org/10.1109/TAES.2016.7812871.

Wei, E., Jin, S.G., Zhang, Q., Liu, J., Li, X., Yan, W., 2013. Autonomous navigation of Mars probe using X-ray pulsars: modeling and results. Adv. Space Res. 51 (5), 849–857. https://doi.org/10.1016/j.asr.2012.10.009.

Winternitz, L.M., Mitchell, J.W., Hassouneh, M.A., Valdez, J.E., Price, S.R., Semper, S.R., Gendreau, K.C., 2016. SEXTANT X-ray Pulsar Navigation demonstration: flight system and test results. In: Aerospace Conference, 2016 IEEE, pp. 1–11. https://doi.org/10.1109/AERO.2016.7500838.

Winternitz, L.M., Hassouneh, M.A., Mitchell, J.W., Valdez, J.E., 2015. X-ray pulsar navigation algorithms and testbed for SEXTANT. In: Aerospace Conference, 2015 IEEE, vol. 2015, pp. 1–14. https://doi.org/10.1109/AERO.2015.7118936.

Wu, L., Tian, X., Ma, J., Tian, J., 2010. Underwater object detection based on gravity gradient. Geosci. Rem. Sens. Lett. IEEE 7 (2), 362–365. https://doi.org/10.1109/LGRS.2009.2035455.

Wu, L., Wang, H., Chai, H., Zhang, L., Hsu, H., Wang, Y., 2017. Performance evaluation and analysis for gravity matching aided navigation. Sensors 17 (4), 769. https://doi.org/10.3390/s17040769.

Yan, J., Yang, X., Ye, M., Li, F., Jin, W., Barriot, J.P., 2017. Independent mars spacecraft precise orbit determination software development and its applications. Astrophys. Space Sci. 362 (7), 123. https://doi.org/10.1007/s10509-017-3105-0.

Yan, J., Yang, X., Ye, M., Li, F., Jin, S., Jin, W., Barriot, J.P., Li, H., 2018. New tracking modes and performance for Mars spacecraft orbit determination and lander positioning. Planet. Space Sci. 163, 5–13.

Zheng, S., Ge, M., Han, D., Wang, W., Chen, Y., Lu, F., He, J., 2017. Test of pulsar navigation with POLAR on TG-2 spacelab. SCIENTIA SINICA Physica. Mech. Astron. 47 (9) https://doi.org/10.1360/SSPMA2017-00080, 099505.